The petrology of the Ozerki meteorite constrained by electron backscatter diffraction and X-ray computed tomography

Alice MACENTE [1,2,3]*, Luke DALY [3,4,5], Sammy GRIFFIN [3], Maria GRITSEVICH[6,7,8],
Jarmo MOILANEN[6,7], Josh Franz EINSLE [3], Patrick TRIMBY[9], Chris MULCAHY[10],
Jonathan MOFFAT[10], and Alexander M. RUZICKA[11]

[1]School of Civil Engineering, University of Leeds, Leeds, UK
[2]Department of Civil and Environmental Engineering, University of Strathclyde, Glasgow, UK
[3]School of Geographical and Earth Sciences, University of Glasgow, Glasgow, UK
[4]Australian Centre for Microscopy and Microanalysis, The University of Sydney, Sydney, New South Wales, Australia
[5]Department of Materials, University of Oxford, Oxford, UK
[6]Faculty of Science, University of Helsinki, Helsinki, Finland
[7]Finnish Fireball Network, Helsinki, Finland
[8]Institute of Physics and Technology, Ural Federal University, Ekaterinburg, Russia
[9]Carl Zeiss Limited, Cambourne, UK
[10]Oxford Instruments Nanoanalysis, High Wycombe, UK
[11]Department of Geology and Cascadia Meteorite Laboratory, Portland State University, Portland, Oregon, USA

*Correspondence
Alice Macente, School of Civil Engineering, University of Leeds, Leeds, UK.
Email: alice.macente@gmail.com

Abstract–Combining electron backscatter diffraction (EBSD) with X-ray computed tomography (XCT) offers a comprehensive approach to investigate shock deformation and rock texture in meteorites, yet such integration remains uncommon. In this study, we demonstrate the synergistic potential of XCT and EBSD in revealing deformation metrics, thereby enhancing our understanding of petrofabric strength and shock-induced deformation. Our analysis focuses on the Ozerki (L6, S4/5, W0) meteorite fall, which was instrumentally observed on June 21, 2018, and subsequently recovered by the Ural's branch of the Russian Fireball Network (UrFU) recovery expedition a few days later. The trajectory analysis conducted by the Finnish Fireball Network facilitated the prompt retrieval of the meteorite. We show that Ozerki is deformed, with a moderate strength foliation fabric defined by metal and sulfide grain shapes. Microstructural analysis using EBSD shows that the parent body was likely still thermally active during this impact event. Our data suggest that these microstructures were likely produced during an impact while the Ozerki's parent body was still warm.

INTRODUCTION

Ordinary chondrites are the most common meteorite type present in worldwide collections (Weisberg et al., 2006). They make up about 77% of all registered meteorites (https://www.lpi.usra.edu/meteor/). Ordinary chondrites are likely to be the building blocks of terrestrial planets and preserve evidence of both thermal heating from the decay of short-lived cosmogenic radionuclides and impact processes during the early solar system (Dodd, 1969; Kallemeyn et al., 1989; Stöffler et al., 1991; Wasson, 1972). They are classified into three major groups based on their iron content and oxidation state: H (high iron), L (low iron), and LL (characterized by their relatively low abundance of metallic iron-nickel).

X-ray computed tomography (XCT) analysis of metals, sulfides, and chondrules in chondrites, specifically ordinary chondrites, has been shown to be an effective tool to understand the shock deformation and the formation of rock fabrics resulting from hypervelocity impacts (Almeida, 2018; Benedix et al., 2008; Friedrich et al., 2008; Gattacceca et al., 2005; Hanna et al., 2015, 2022; Hanna & Ketcham, 2017; Krzesińska, 2011; Lindgren et al., 2015; Martell et al., 2022). At the same time, electron backscatter diffraction (EBSD) is a powerful technique to evaluate impact deformation, rock textures, and to infer the environmental conditions present during deformation, such as temperature, pressure, strain rate, and water content (Daly, Lee. et al., 2019; Forman et al., 2017, 2019; Goudy et al., 2023; Hugo et al., 2020; Jung et al., 2006; Karato et al., 2008; Luo et al., 2024; Ruzicka et al., 2024; Ruzicka & Hugo, 2018). Despite their relative complementary strengths to evaluate deformation, they have been rarely used in a correlative manner on meteorites. Here, we applied both techniques to a subsample of the Ozerki meteorite to evaluate the rock microstructures and impact history.

The Ozerki meteorite is an L6 ordinary chondrite (Gattacceca et al., 2020; Kartashova et al., 2020; Korochantseva et al., 2020; Maksimova et al., 2020). Its fall was widely observed as an exceptionally bright fireball occurring at 01:16:20 UT on June 21, 2018 (Kartashova et al., 2020; Maksimova et al., 2020; Pastukhovich et al., 2019). This event was captured by numerous stationary and mobile cameras not only in Lipetsk but also in the Oryol, Kursk, and Moscow regions of Russia, as well as in the Kharkiv and Cherkasy regions of Ukraine. Building on the successes of previous joint projects that led to the recovery and analysis of Annama and Chelyabinsk meteorites (Gritsevich, Lyytinen, Kohout, et al., 2014; Gritsevich, Lyytinen, Moilanen, et al., 2014; Kohout et al., 2014, 2017), a collaborative effort between researchers from the Ural's branch of the Russian Fireball Network (UrFU) and the Finnish Fireball Network was initiated to analyze the fireball trajectory and facilitate meteorite recovery. The calibration of cameras and trajectory triangulation followed methodologies outlined in Lyytinen and Gritsevich (2016a, 2016b), and Gritsevich et al. (2024). An analysis of the fireball trajectory (Gritsevich, 2007, 2009, 2013), with accounts for the atmospheric conditions (Lyytinen & Gritsevich, 2016b), strongly indicated the survival of meteorite fragments through atmospheric entry (Gritsevich et al., 2012). Subsequently, a strewn field was computed using the DFMC model to estimate the distribution of these fragments (Moilanen et al., 2021). With the support of this knowledge, a search expedition was organized within 2 days of the meteorite fall (Maksimova et al., 2020). The UrFU-led expedition achieved its nearly immediate success on June 25, 2018,

recovering the first fragment in the predicted strewn field area 4 days after the sighting of the fireball.

The Ozerki meteorite fragments have a moderately high shock classification of S4/5 evidenced by undulatory extinction, planar and irregular fractures in olivine, as well as the presence of shock melt veins (Gattacceca et al., 2020; Stöffler et al., 1991). Recovered within days since the fireball and deployment of the search expedition, the meteorite exhibits minimal terrestrial weathering as evidenced by the absence of oxidized rims around metal grains, and as such its weathering grade is W0 (Gattacceca et al., 2020; Maksimova et al., 2020). The Ozerki meteorite is comprised of a silicate matrix, with relict chondrules of olivine and pyroxene, metal grains (as Fe-Ni-Co alloys), chromite grains and troilite, dispersed in the matrix (Maksimova et al., 2020). Troilite grains have been described to have a high amount of porosity in the interior (Maksimova et al., 2020).

Meteorite falls that have been instrumentally observed are becoming increasingly important to our understanding of solar system evolution (Devillepoix et al., 2020; Jenniskens, 2018; Kyrylenko et al., 2023; Meier et al., 2017; Trigo-Rodríguez et al., 2015). This is because (1) the observations of the fireball can be used to determine the meteoroid's pre-atmospheric orbit and therefore provide insights into its origin in space, linking meteorites to asteroids and providing the geological context that is typically absent from meteorite finds (Devillepoix et al., 2020; Dmitriev et al., 2015; Gritsevich et al., 2024; Jenniskens, 2018; Peña-Asensio et al., 2021), and (2) the observed meteorite falls are typically recovered quickly (days-years) so have minimal terrestrial contamination and alteration compared to meteorite finds (Devillepoix et al., 2020; King et al., 2022; Maksimova et al., 2020; Russell et al., 2023; Sansom et al., 2019).

These valuable insights into solar system evolution from meteorite falls are amplified with advances in 2-D and 3-D correlative microstructural analysis and non-destructive imaging techniques (Hanna & Ketcham, 2017; Martell et al., 2022; McCarroll et al., 2022; Zolensky & Mikouchi, 2010). These novel approaches are steadily replacing traditional qualitative petrological observations, descriptions, and interpretations of a given meteorite's geological history with quantitative measurements of the meteorite's texture. Quantitative observations are also being supported by laboratory experiments to constrain the precise environmental conditions the meteorite experienced (Karato et al., 2008; Miyahara et al., 2021; Tomeoka et al., 1999). Of particular interest is the shock metamorphic history of meteorites and peak shock pressure/temperature experienced by the sample (Friedrich et al., 2008; Hugo et al., 2020; Kohout et al., 2014; Lindgren et al., 2015; Miyahara et al., 2021; Ruzicka & Hugo, 2018; Stöffler et al., 1991, 2018; Tomeoka et al., 1999). Meteorites are

typically ascribed as a shock stage (S1-S6/7) that is traditionally established using optical petrology to describe microstructures within minerals that are unique to hypervelocity impact zones and form at specific shock pressures (Stöffler et al., 1991, 2018). Recently, it has been shown that similar classification systems can be established for meteorites, particularly chondritic meteorites using XCT to determine the 3-D petrofabric of metal grains (Friedrich et al., 2008; Hanna & Ketcham, 2017) and EBSD to measure the internal deformation and overall internal misorientation relationships to infer the ambient temperature and amount of annealing (Hugo et al., 2020; Ruzicka et al., 2024; Ruzicka & Hugo, 2018).

For this study, we combined EBSD and XCT to determine the petrology of the Ozerki meteorite fall, with a particular focus on the 3-D shape of metal, chromite, and troilite grains as well as the microstructure of olivine grains. We are particularly interested in understanding whether the metal, sulfide, and oxide phases have any 3-D textural and orientation relationships, and in determining their fabric strength, as defined by Woodcock and Naylor (1983), Friedrich et al. (2008), Friedrich and Rivers (2013), and Hanna and Ketcham (2017), alongside other measures of 3-D and 2-D fabric strength. In addition, we determine the average olivine grain deformation and predominant active olivine slip systems to evaluate the strain–temperature relationships, as outlined by Ruzicka and Hugo (2018) and Ruzicka et al. (2024). Both these quantitative metrics have been shown to link to the shock classification (Hanna & Ketcham, 2017; Ruzicka & Hugo, 2018). We examine both techniques in tandem on the Ozerki meteorite sample to assess the magnitude of shock it underwent. Additionally, our aim is to establish a correlation between these methods, offering insight into the extent of shock-induced deformation.

METHODOLOGY

Sample Preparation

A 2 cm^3 fragment of the Ozerki meteorite was embedded in a one-inch round sample mount with epoxy resin. One side of the sample was polished flat using an iterative series of polishing mats from 10 µm diamond to 1 µm diamond with distilled water. To prepare the sample side for EBSD analysis, the sample was further polished in a 1 and 0.3 µm suspension of Al spheres in distilled water for 15 min each. The sample was then chemically polished using a suspension of colloidal silica in NaOH solution on a vibratory polisher (Buehler Vibromet) for 4 hours. To minimize any alteration induced by long-duration exposure to water, the sample was dried and stored in a desiccator with oxygen scavengers. No

evidence of terrestrial alteration was observed in the sample during analysis. The sample was coated with 5 nm of carbon and grounded to an Al stub using silver paint.

X-Ray Computed Tomography

The same fragment was then scanned in the XCT facility hosted in the University of Strathclyde, using a Nikon XT H 320 LC system. The scan was acquired using a transmission source, a beam energy of 140 kV, and a beam current of 58 µA. Over a 360° rotation, 3141 projections were acquired, one frame per projection, with an exposure time of 1.42 s per each frame. A Cu filter of 0.25 mm thickness was inserted between the source and the sample to minimize beam hardening artifacts. The acquired scan was reconstructed using the Nikon proprietary software. The final reconstructed voxel size was 11.13 µm. Digital image processing of the data was carried out using Avizo®. The data are represented by gray scale values, which relate to the densities and composition of the material that is being analyzed. Denser minerals appear as bright voxels, while less dense materials (e.g., air) appear as dark voxels (Figure 1) (Baker et al., 2012; Ketcham & Carlson, 2001). Metal and troilite grains appear to have significantly different intensities, while chromite and troilite grains have very similar intensities and are therefore grouped together. However, because of partial volume effects, the outer edges of the metal grains present similar intensities to the troilite
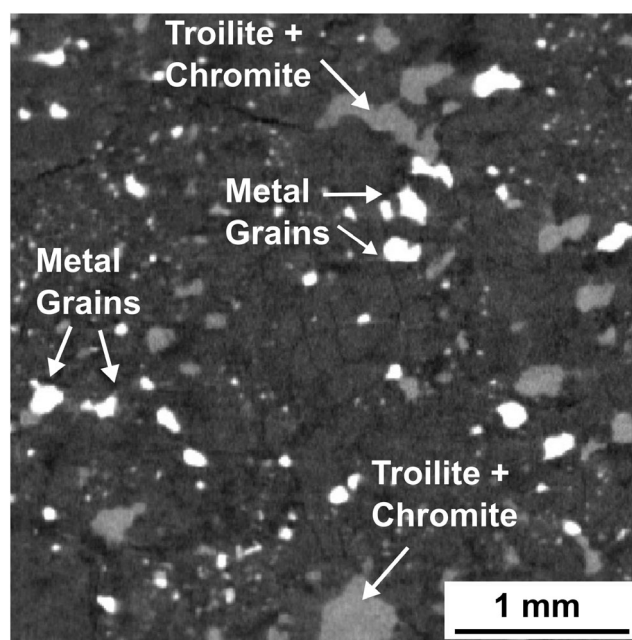

FIGURE 1. XCT XZ vertical slice, showing the distribution of the mineral phases. Highlighted by the white arrows are the Fe-metals grains (high attenuation phases) and troilite + chromite grains (moderate attenuation phases).
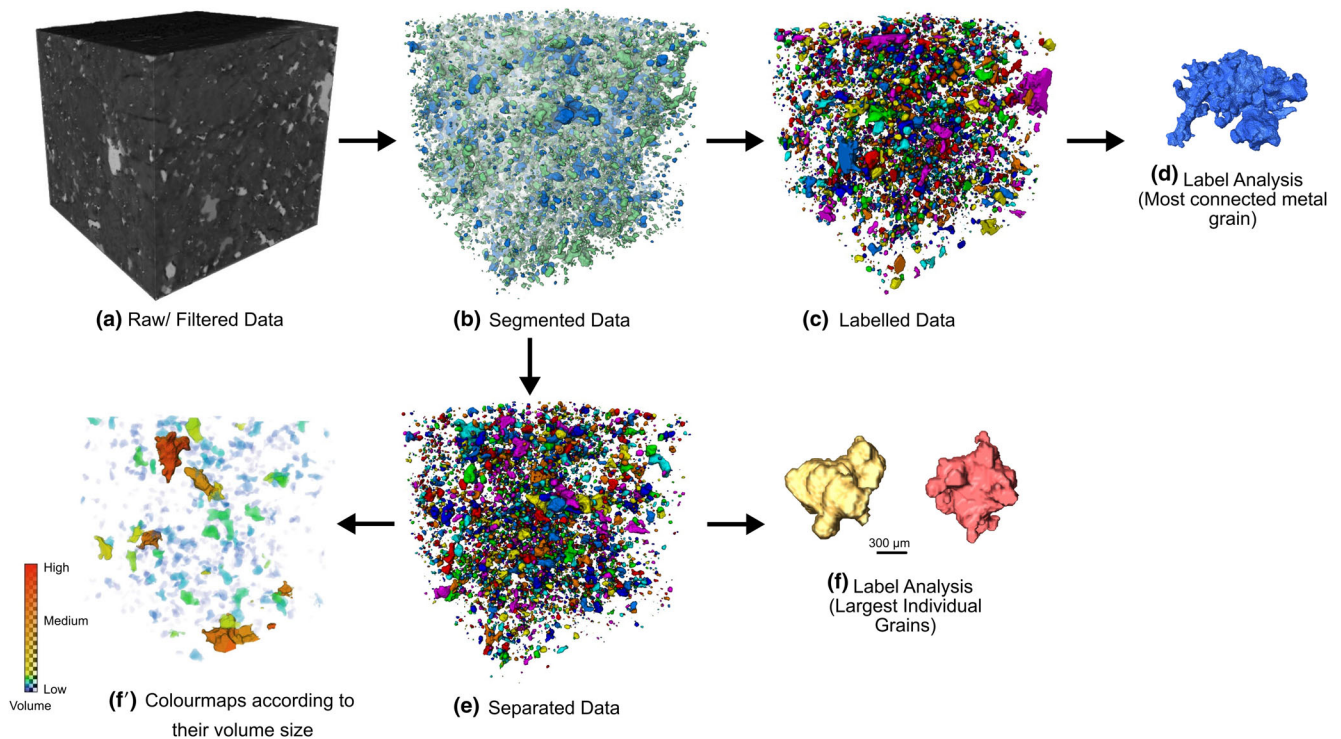
FIGURE 2. Schematic workflow representing the steps for data processing using 3-D volume renderings: (a) Filtered data of raw images. (b) Segmentation of the two phases after applying the Trainable Weka Algorithm. (c) Label analysis for interconnectivity and (d) identification of largest connected cluster. (e) Separation of individual grains after segmentation. (f) Label analyses to look for volume, shape, and orientation analyses and (f') 3-D volume rendering of the grains, coloring based on volume size determined by (f).

and chromite. Because of this overlapping, it was not possible to choose a simple thresholding method for the segmentation as this would introduce significant errors in the quantification. We chose to apply a machine-learning (ML) algorithm instead. The XCT data were first filtered for noise using the anisotropic diffusion filter in 3-D, that comprised five iterations (Perona & Malik, 1990). Then, the filtered data were imported into ImageJ, and the Trainable Weka Algorithm (ML) was applied to perform segmentation (Arganda-Carreras et al., 2017). Because the ML algorithm segment phases based not only on intensities but also by recognizing characteristics belonging to the phase, the resulting segmentation is optimized and errors minimized. The workflow adopted in this study is summarized in Figure 2.

Segmented data were then imported in Avizo for post-processing. First, a mask was generated that excluded the air outside of the sample which acts as a reference volume for the quantification. A majority filter ($3 \times 3 \times 3$) was applied to clean up the images. Volume percentage of the phases was calculated using the volume fraction operator. Subsequently, the interconnectivity of the phases was verified through labelling and label analysis. For the label analyses, a lower threshold of 125 voxels was chosen. This defines the smallest resolvable particle or volume for

consideration which is 0.000172 mm³. Individual grain size distribution analyses were also performed on the Fe-metal grains and troilite + chromite phases. After segmentation, a separate object operator was used with a kernel size 1, and a neighborhood 6, to separate the segmented objects into individual grains. The labeled and separated grains data were then imported in *BoneJ* to determine orientation and shape descriptors. Orientations and shape descriptors, as well as equivalent diameter and volumes, were then calculated for each individual grain. Orientations of the major, intermediate, and minor axes of the best-fit ellipsoid were extracted from *BoneJ* analyses for the two mineralogies. The data were then imported in python, and lower hemisphere equal-area stereographical projections were calculated using the library mplstereonet (https://github.com/joferkington/mplstereonet). Contours were calculated using the exponential Kamb method, with sigma values set to replicate the same color bar and contouring across different data points. The strength parameter C and shape parameter K have been calculated in *OpenStereo*, following methods by Woodcock and Naylor (1983), Friedrich et al. (2008), Friedrich and Rivers (2013), and Hanna and Ketcham (2017). The strength parameter C is defined as: $\ln \frac{S_1}{S_3}$, where S_1 and S_3 are the eigenvalues of the grains, and it defines the strength of the preferred

orientation: the larger the C, the stronger the preferred orientation. The shape parameter K is defined as: $\frac{\ln S_1/S_2}{\ln S_2/S_3}$; $K < 1$ defines a girdle distribution indicating a foliation, while $K > 1$ defines a cluster distribution indicating a lineation. These values are plotted in the eigenvalue ratio graph, where random distribution would plot close to the zero axis, with low C values (Woodcock & Naylor, 1983). We also plotted the same values in Vollmer diagrams in *OpenStereo*. Vollmer diagrams are used to represent the principal values (eigenvalues) of the orientation tensor into a distribution, divided into three: point or cluster (P), girdle (G), and random (R) or uniform distribution (Vollmer, 1990). Random or uniform distribution represents weak fabrics, whereas any component toward a girdle or a point represents moderate to strong foliation or lineation, respectively.

Individual grain shape analyses were calculated using Flinn diagrams. Flinn diagrams are created by plotting the log ratio between the eigenvalues (L1, L2, L3) of the inertia moments of the best-fit ellipsoid for each particle. Depending on where the data points distribute in the graph, this graph provides information on the type of deformation experienced by the grains, and it can distinguish between prolate ellipsoids, which have experienced constriction deformation, and oblate ellipsoids, which have experienced flattening. Isotropic deformation is located at 0 degrees of deformation, while any triaxial deformation is located along the plain strain ($k = 1$) isoline at the top right corner of the Flinn diagram (Figure 6). Orientations and shape analyses have been calculated for volumes larger and smaller than 5000 voxels ($\sim$0.007 mm^3), to compare any effect given by size as grains with a volume smaller than 5000 voxels appeared to have the greatest influence on our data analyses.

Scanning Electron Microscopy and Electron Backscatter Diffraction

To aid in robustly defining phases and inform the interpretation of the XCT data, the exposed surface of the sample was also analyzed by scanning electron microscopy (SEM), energy-dispersive X-ray spectrometry (EDS), and electron backscatter diffraction (EBSD) techniques. SEM data including backscatter electron (BSE) images, EDS chemical maps, and EBSD data were acquired on a Zeiss Sigma variable pressure field emission gun (VP-FEG) SEM equipped with a NordlysMax^2 EBSD detector and an X-Max 80 mm^2 silicon drift energy-dispersive X-ray spectrometer from Oxford Instruments. BSE images and EDS maps were acquired at a horizontal tilt angle with an accelerating voltage of 20 kV and a beam current of 4.1 nA. EBSD data were collected at a tilt angle of 70° and the same electron beam conditions. Large area EBSD maps were collected at a

step size of 4 μm over a 9 × 11 mm area. High-resolution EBSD maps were acquired using a step size of 0.3–0.6 μm. Additional EBSD data were acquired using a Tescan Mira 3 FEG SEM at Oxford Instruments Nanoanalysis High Wycombe equipped with an Ultim Max 170 mm^2 EDS detector and the CMOS-based symmetry EBSD detector. The operating conditions used for this SEM were 20 kV. EBSD maps obtained with the Symmetry detector were collected at a 70° tilt angle with step sizes ranging from 1.9 to 0.75 μm. The phases chosen for EBSD analysis are awaruite for metal grains and troilite for sulfide grains. Phase information on olivine, chromite, clinopyroxene, orthopyroxene, and feldspar was also collected. The mean angular deviation, which is a metric that indicates the quality of the EBSD pattern indexing process, where <1 is considered good, was an average of 0.40 for Fe-Ni-metal and 0.52 for olivine. EDS and EBSD data were collected using the Aztec 3.4 software package and interpreted using the AztecCrystal 1.1 software package from Oxford Instruments. The EBSD data were denoised using a wildspike correction followed by an iterative 6-point nearest neighbor correction. The wildspike correction did not affect our results. The plane of the SEM/EBSD analyses, pole figures, and rose diagrams were rotated and overlain onto the same plane of reference inside the XCT data, enabling a direct correlation between these data sets (Figure 3a). Grain boundaries within the EBSD data were defined by $>10°$ misorientation across adjacent pixels. To avoid grain artifacts from small/poorly characterized grains, only grains defined by >50 pixels were included to assess deformation microstructures and shape fabrics to ensure that the shape and crystallographic orientations are robustly measured, given our step size of 4 μm, this equates to a minimum circle equivalent diameter of 32 μm. Fifty pixels was chosen as a lower limit for grain size as, below that, multiple grains have near identical size and shapes suggesting a spatial resolution limit, while above 50 pixels grain size varied following a natural variation. It should be noted for comparability that Ruzicka and Hugo (2018) only considered grains >50 μm and did not use any data cleaning protocols. We chose to use number pixels as a more robust evaluation of grain size shape and orientation which is also independent of the step size used, as well as chose to clean the data to provide a clearer picture of deformation microstructures. For consistency, we also produced a second set of analyses using no data cleaning and a 50 μm circle equivalent diameter grain size limit in line with Ruzicka and Hugo (2018) and found the results were very similar regardless of the data processing approach. From this population of grains, we calculated the maximum orientation spread which gives the maximum difference in orientations between two pixels within each grain and
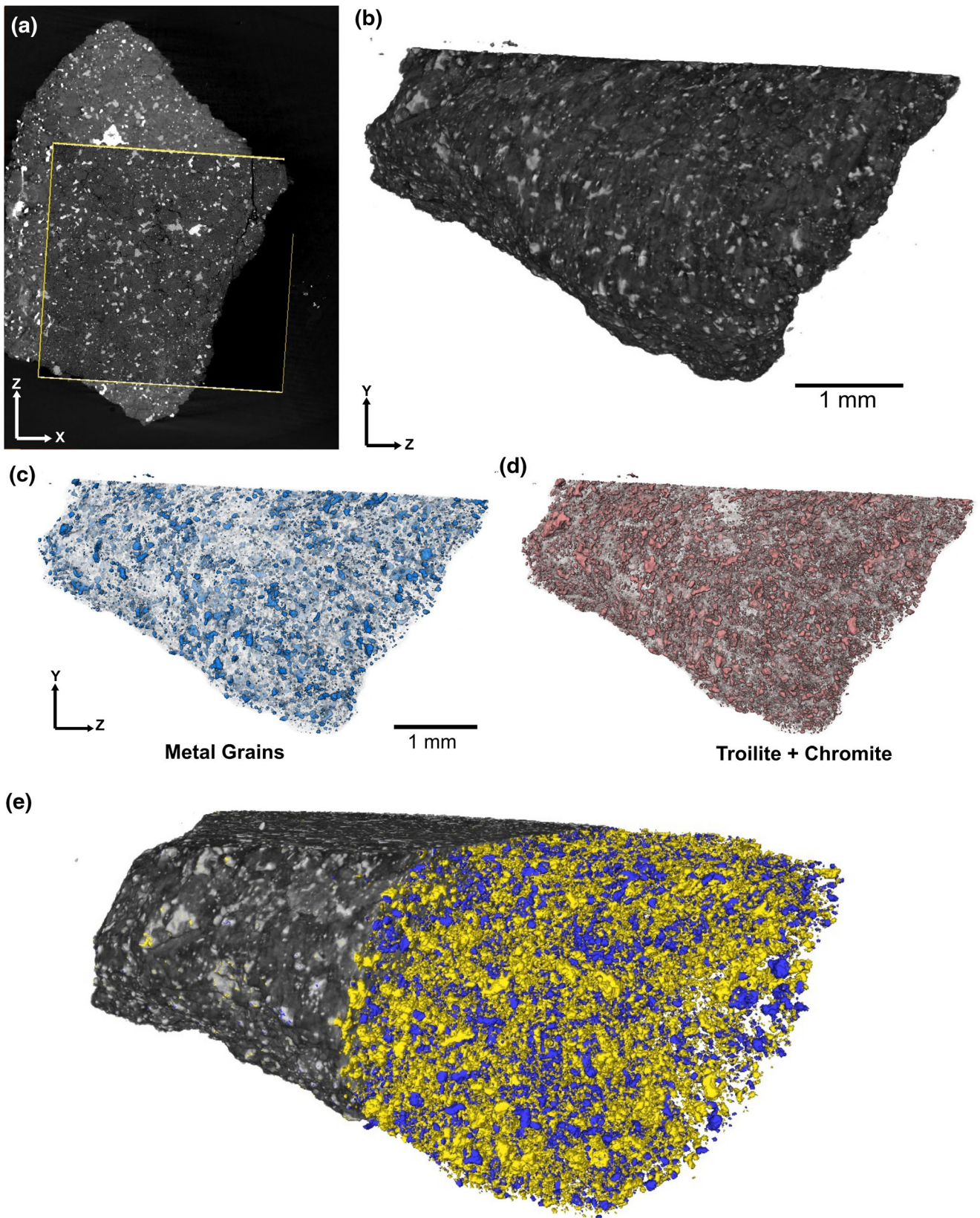
FIGURE 3. (a) X-ray tomographic slice (XZ plane) and SEM backscattered image (yellow outline) overlaid together to show the correlation between the two techniques. Gray-scale original data contained in Figure 1 for reference. (b) 3-D volume rendering of the scanned sample. (c, d) Segmented metal grains and troilite + chromite grains, respectively, after applying the Trainable Weka Algorithm. Matrix is rendered in white foggy opaque color. (e) 3-D volume renderings of metal (blue) and troilite + chromite (yellow) grains on the sample, here rendered in gray values on the other half of the image. The top plane corresponds to the sectional plane of EBSD and BSE SEM images.

mean orientation spread which is the average misorientation between pixels within each grain. These data provide insight into the severity of the deformation and the pervasiveness of the deformation, respectively. To compare deformation across the grain population, we calculated the average and median mean orientation spread of the grain population (typically referred to as grain orientation spread—GOS, Brewer et al., 2009), and the average and median maximum orientation spread of the grain population (typically referred to as MOS).

We also generated a grain reference orientation deviation (GROD) angle map for these EBSD data. A GROD-angle map is produced by taking the average crystallographic orientation of every pixel within each grain and then color coding the pixels within that grain relative to that average, where cooler colors reflect parts of the grain that are close to or the same as the average (undeformed) while warmer colors reflect larger misorientations away from that average (more deformed). As such, GROD angle maps are an excellent way to visualize internal misorientation within grains. The long shape axis of metal grains was determined using a best-fit ellipsoid. The crystallographic texture of metal grains and olivine was visualized by extracting one orientation point per crystallite (from a randomly selected pixel within each grain), to remove bias from larger grains, and plotting the crystallographic orientations on a lower hemisphere stereographic projection with density contours using a 5° half width followed by a smoothing function. Quantitative textural metrics m-index and j-index as well as eigenvalue analyses were calculated for the crystallographic orientations of the olivine and metal grains (Daly, Piazolo, et al., 2019; Griffin, Daly, Keller, et al., 2022; Skemer et al., 2005). The M-index is a measure of fabric strength which is based on the distribution of misorientation angles of the sample compared to a theoretical random fabric. As such, an M-index spans a range of values from 0 to 1, where 0 represents a random fabric and 1 represents a single crystal (i.e., everything grain is perfectly aligned with each other). The J-index is also a measure of fabric strength but is defined by the distribution of orientations of a specific crystal axis and ranges from 1 (random fabric) to infinity (single crystal). To investigate the environmental conditions during the deformation of Ozerki, mesoscale slip systems of olivine were determined by plotting crystal rotation axis diagrams for forsterite for pixel-to-pixel misorientations within each grain that range between 2

and 10°. 2–10° was chosen as 10° is the definition of a grain boundary, and 2° was chosen as a value substantially above the angular resolution (0.5°) of the EBSD technique (Sneddon et al., 2016), and this range has been shown to provide more discerning information about slip systems by Ruzicka and Hugo (2018). The crystal rotation axis diagrams were contoured to determine multiples of uniform density (MUD) using a 25° half width, followed by a smoothing function in line with the approach of Ruzicka and Hugo (2018) and Ruzicka et al. (2024). Specifically, the crystal rotation axis diagrams were used to determine a parameter that has been dubbed R2-10, based on intergranular misorientations in olivine (defined by misorientation rotation axis directions in an olivine crystal frame), which can be related to slip systems and deformation temperatures, where higher R2-10 values correspond to higher deformation temperatures (Ruzicka et al., 2024; Ruzicka & Hugo, 2018). For both pole figures and crystal rotation axes, MUD values progressively >1 indicate greater prevalence and values progressively <1 indicate greater deficiency, relative to a uniform spatial distribution. Slip systems in olivine can also be inferred using the Weighted Burgers Vector (WBV) technique described by Wheeler et al. (2009, 2024). Weighted Burgers vectors (WBVs) for low angle boundaries (<5°) were calculated and plotted to highlight potential slip directions.

RESULTS

X-Ray Computed Tomography

XCT analyses reveal that the order of the X-ray linear attenuation decreases from metal grains to troilite + chromite, to the silicate matrix composed of relict chondrules of olivine and pyroxene, meaning that the brightest phases in the reconstructed data are the Fe-metal grains and troilite + chromite (Figures 1 and 3). The volume analyses revealed that the metal grains account for ~3.1% in volume, while the troilite + chromite grains account for ~5.4% of the volume of the sample (Figure 3c–e).

Label analyses on segmented data have been conducted to investigate the connectivity of the grains for both phases. Most connected clusters are distributed in volumes larger than $10^6 \, \mu m^3$ (or $0.001 \, mm^3$) for both phases. The largest metal grain cluster ($5.12 \times 10^8 \, \mu m^3$ or $0.5 \, mm^3$) constitutes 1.8 vol% of the total metals present
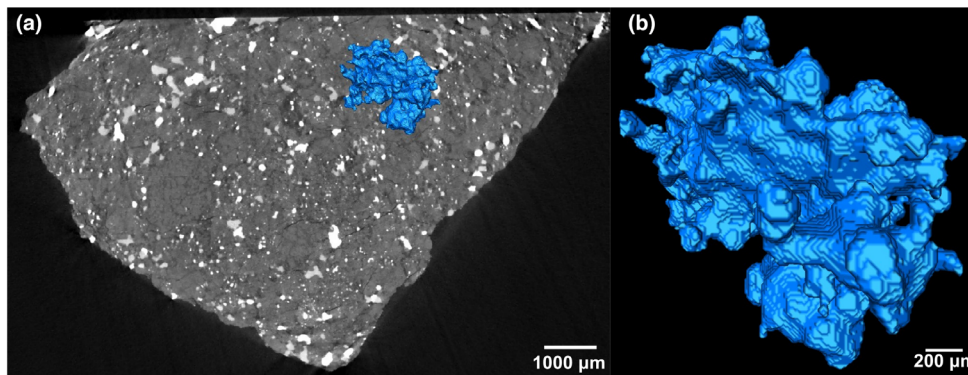
FIGURE 4. Largest connected cluster of metal phase within the sample (a) and rendered in 3-D (b): note that the cluster is composed of individual grains, which are thoroughly connected to each other.
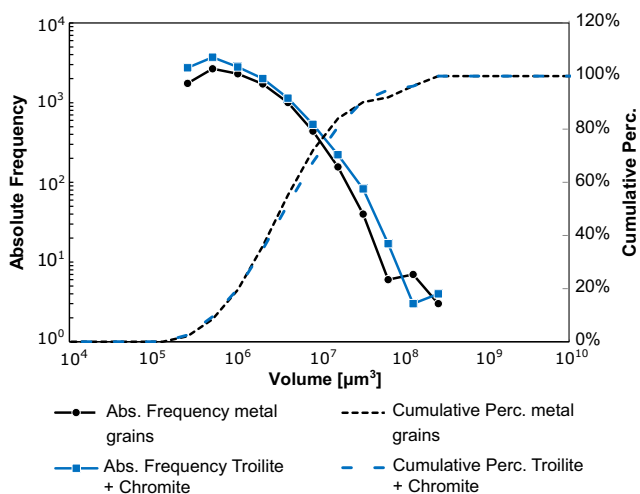

FIGURE 5. Grain size frequency distribution for metal phases and troilite + chromite phases. Cumulative frequency curves are also reported. The two phases display similar grain size distribution, with troilite + chromite being characterized by a larger number of grains per size class overall.

in the meteorite and only 0.06 vol% of the sample (Figure 4). Connected metal clusters larger than $10^6 \, \mu m^3$ account for 75.5% of the totality of metal phases (Figures 4 and 5). In contrast, the distribution of troilite + chromite is characterized by more than twice the number of labels compared to the metal grains. Of these troilite + chromite labels, the largest one occupies a volume of $4 \times 10^8 \, \mu m^3$ (0.4 mm^3), constituting 0.9% of the totality of troilite + chromite content and only 0.05 vol. % of the sample volume.

Individual grains have been analyzed by using the *BoneJ* operator for shape and orientation analyses. We plotted the frequency of the grain sizes divided into bins by the power of 2 (Figure 5). The grain size analysis reveals that 76% of metal grains are distributed in small volumes, ranging from $5.2 \times 10^5 \, \mu m^3$ to $3.36 \times 10^7 \, \mu m^3$

(Figure 5). The largest metal particle has a volume of $2.3 \times 10^8 \, \mu m^3$ (0.22 mm^3) (as shown in Figure 4). Troilite + chromite grains account for 81% in volumes ranging from $5.2 \times 10^5 \, \mu m^3$ to $3.36 \times 10^7 \, \mu m^3$. The largest troilite + chromite grain has a volume of $2.3 \times 10^8 \, \mu m^3$ (0.22 mm^3) (Figure 5). Both metal and troilite + chromite phases show a similar distribution. However, troilite + chromite shows a higher absolute frequency of grains overall (Figure 5). The cumulative frequency curves do not show any major difference between metal and troilite + chromite, and the grain size distribution curves are also very similar (Figure 5).

Shape analyses were obtained by plotting eigenvalues of the individual grains in Flinn diagrams (Figure 6). The data in the Flinn diagrams have been colored and scaled by their relative grain volume (Figure 6). Both phases seem to present both prolate and oblate grain shapes (Figure 6), with a tendency towards prolate grains in the fine-grained data sets (Figure 6a,c). However, most smaller grains seem to cluster at $k = 0$, indicating that they did not experience much deformation (Figure 6a,c). The coarse-grained data sets do not appear to show any predominant shape preference and have the range of shapes from oblate to prolate (Figure 6b,d).

We plotted the orientations of the maximum, intermediate, and minimum axes of the best-fit ellipsoid on the grains, obtained through *BoneJ* on a stereographic projection (Figure 7). We also calculated the eigenvalues of the best-fit ellipsoids and plotted them on a Vollmer diagram (Figure 8) and an eigenvalue ratio plot (Figure 9). The metal grains and the troilite + chromite grain populations show very similar orientations for their major, minor, and intermediate axes (Figure 7). The values of the strength parameter (C) and shape factor (K) indicate that the major and intermediate axes have weak to moderate preferred orientations and very low (<1) shape values indicative of a foliation (girdle distribution) (Figures 7–9). Additionally, the major axes of the metals
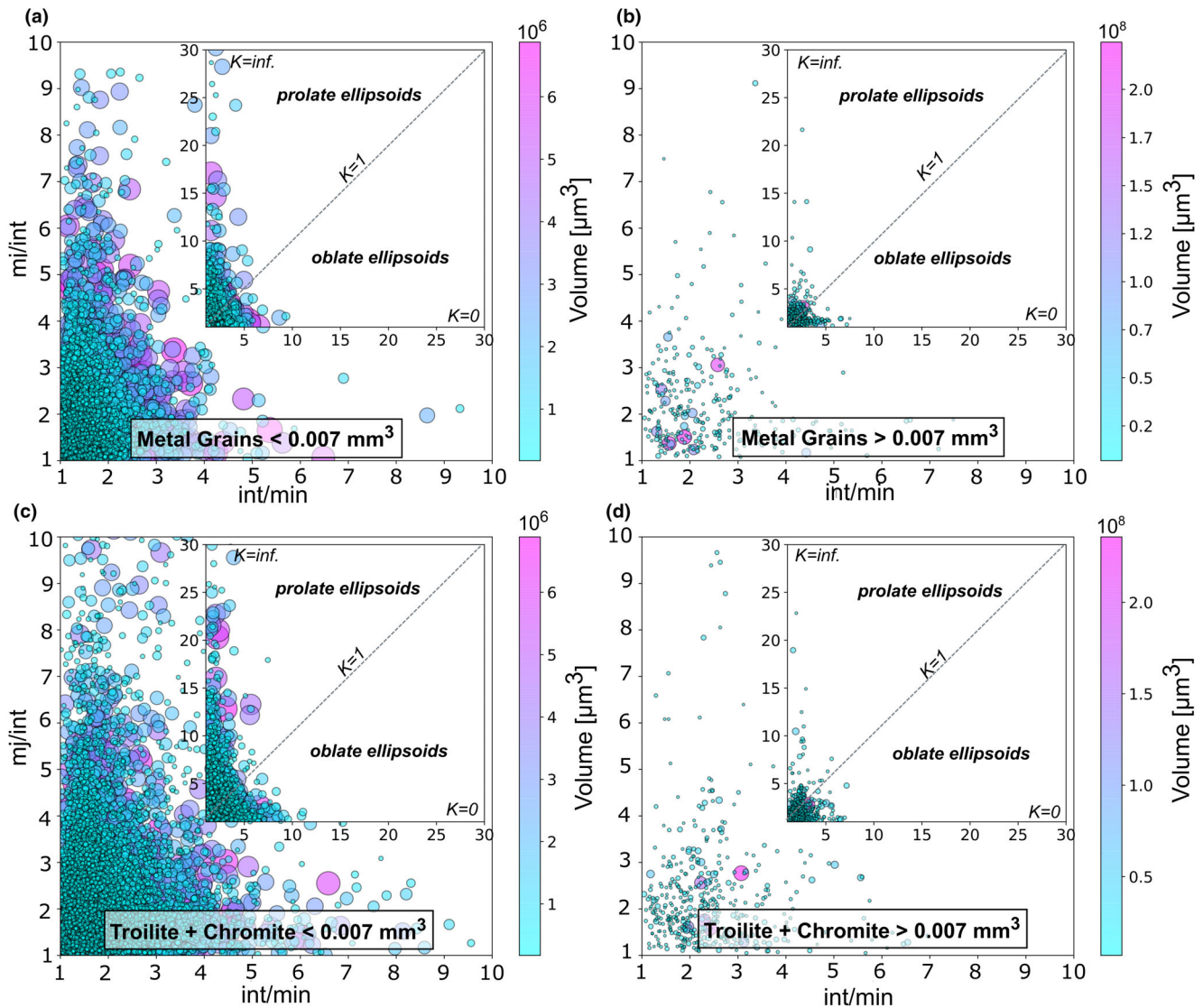
FIGURE 6. Flinn diagrams for metal phases (a, b) and troilite + chromite (c, d), for smaller volume grains (a, c) and larger volume grains (b, d) greater than 5000 voxels (∼0.007 mm³). Data points are scaled and colored according to their volumes (color bar on the right). Zoom-in insets are present for values up to 30, to give a broader overview. Both phases are characterized by a broad spread from prolate to oblate shapes with a preference for prolate appearing in the fine-grained data sets. Mj = major, int = intermediate and min = minor axes.

and troilite + chromite, while still predominantly a girdle fabric, exhibit slightly more of a lineation fabric relative to the intermediate axis (Figure 8). The minor axis, for both phase groups, exhibits a cluster distribution, indicative of a lineation fabric that is also in the same orientation for both phase groups (Figures 7–9). The fabrics present in the coarse-grained data set are systematically stronger than those present in the fine-grained data set (Figures 7–9). Interestingly, the orientation of the coarse-grained data set's lineation of the minor axis is slightly offset to the fine-grained data sets (Figure 7).

EBSD Results

Omitting non-indexed pixels, the processed and "cleaned" EBSD data indicate that the area measured has a modal mineralogy of 74% olivine, 13% pyroxene (orthopyroxene + clinopyroxene indexed pixels), 0.9% troilite, 6.5% feldspar, 3.5% metal grains, and 1.8% chromite (Figure 10a). Pyroxene and feldspar modal mineralogy abundances will be underrepresented due to patchy indexing. Metal grains modal mineralogy derived by EBSD is very similar to that measured by XCT. EBSD data reveal that metal grains are single crystals that are
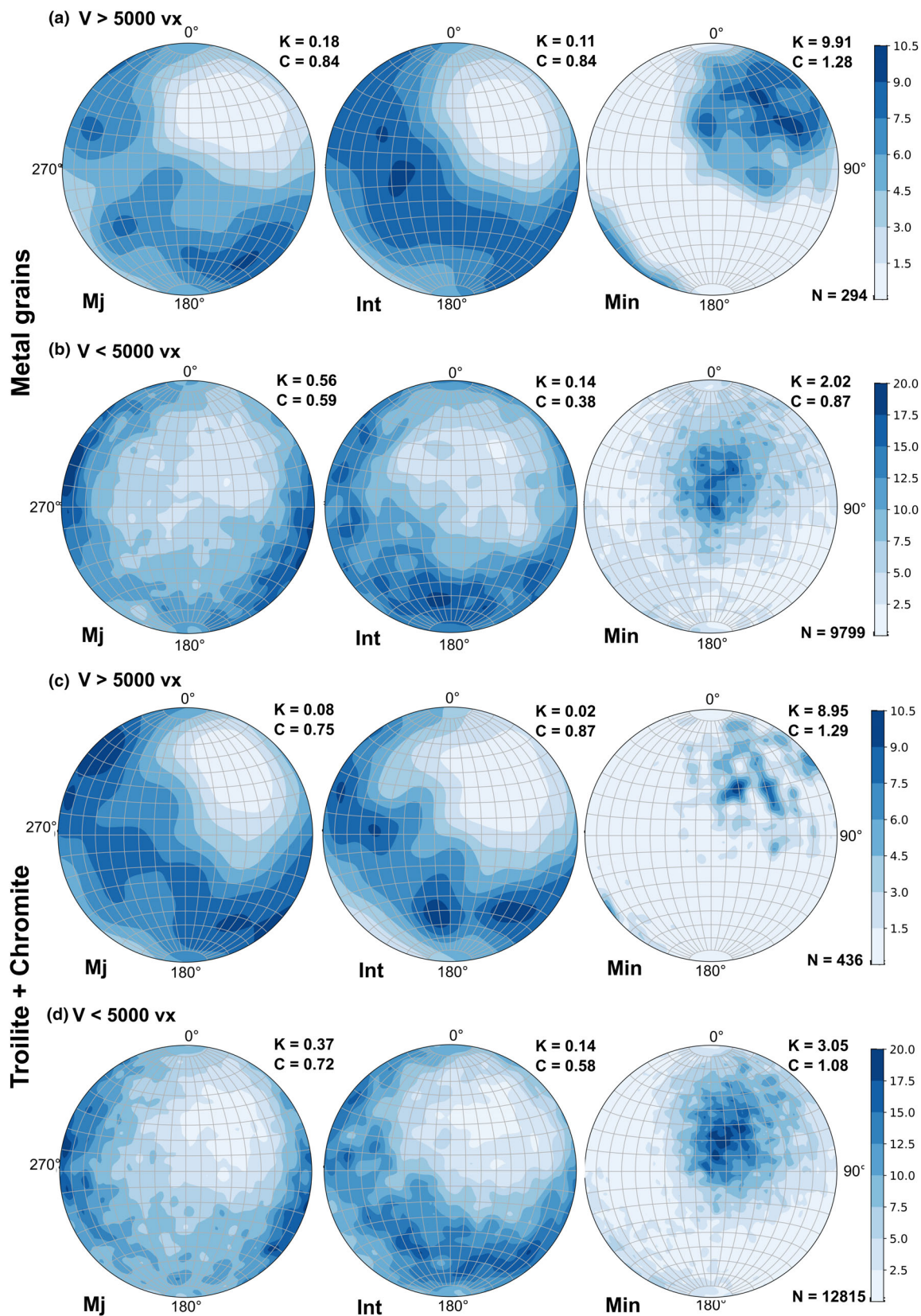
FIGURE 7. Orientations of the major ("mj"), intermediate ("int"), and minor ("min") axes of the best-fit ellipsoid from *BoneJ* analyses for the two phase groups. Orientations have been calculated for volumes larger than 5000 voxels (V > 5000 vx, ~0.007 mm³) (a, c) and smaller (V < 5000 vx, ~0.007 mm³) (b, d) respectively, and they are in the x, y, z reference frame of the XCT data. Contours were calculated using the exponential Kamb method, with sigma values set to replicate the same color bar and contouring across different data points. K and C indicate the shape factor and the strength parameter, respectively, as calculated in *OpenStereo*. N indicates the amount of data points. Note the girdle maxima within the major and intermediate axes and the pole maxima in the minor axes for both size classes.

Coarse - grained data set
■ Metals Major Axis > 5000 vx   ▲ Metals Interm. Axis > 5000 vx   ● Metals Minor Axis > 5000 vx
■ Troilite + Chromite Major Axis > 5000 vx   ▲ Troilite + Chromite Interm. Axis > 5000 vx   ● Troilite + Chromite Minor Axis > 5000 vx

Fine - grained data set
□ Metals Major Axis < 5000 vx   △ Metals Interm. Axis < 5000 vx   ○ Metals Minor Axis < 5000 vx
□ Troilite + Chromite Major Axis < 5000 vx   △ Troilite + Chromite Interm. Axis < 5000 vx   ○ Troilite + Chromite Minor Axis < 5000 vx
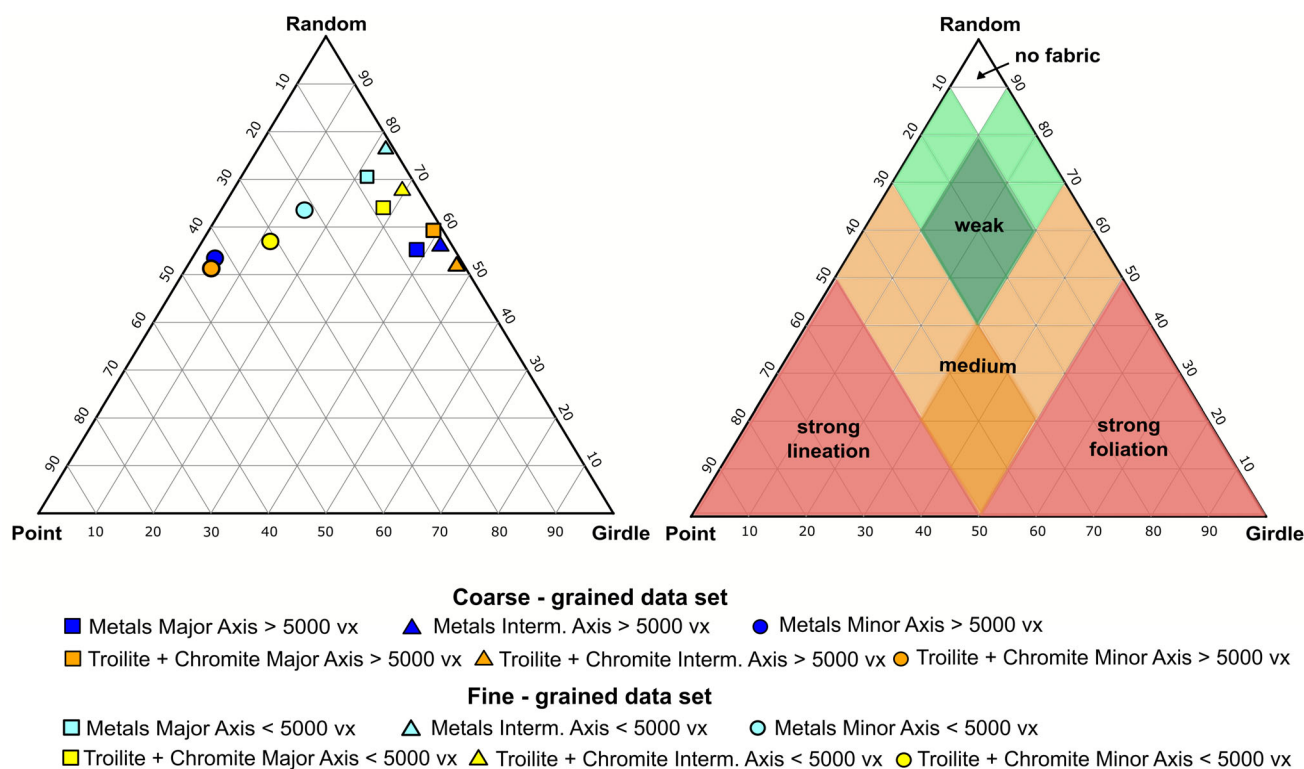
FIGURE 8. Left: Vollmer diagram from *OpenStereo* with the different phase groups and size classes (coarse-grained or fine-grained; larger or smaller than 5000 voxels) represented. Right: Vollmer diagram highlighting where strong or weak orientations plot. Major and intermediate axes for both phase groups and grain size classes plot in a "weak–moderate" strength girdle distribution. The minor axis for both phase groups (metals for metal grains, and troilite + chromite) and grain size classes plot as a "moderate strength" lineation. It should be noted that, while our data plot in areas of the Vollmer graph that are traditionally associated with weak and moderate fabric strengths, that these are usually derived from metallurgical literature where very strong fabric alignments are produced. For geological materials and extraterrestrial samples, even weak to moderate fabrics in this plot should be considered quite strong in nature (Daly, Piazolo, et al., 2019; Griffin, Daly, Keller, 2022; Griffin, Daly, Piazolo, 2022).

highly deformed (Figures 11a and 12l). Metal grain deformation is exhibited by their overall average mean orientation spread of 5.2° and an average maximum orientation spread of 14.7°. In total, 255 metal grains >50 pixels were detected in the large-area EBSD maps (Figure 10c, Table S1). The grain size (defined by the equivalent circle diameter) of the metal grains ranged between 32 and 426 μm with an average grain size of 63 μm. The metal grains are elongated in shape with an average aspect ratio of 1.9. However, it should be noted that these grain size and aspect ratio data are vulnerable

to cutting artifacts and so should be taken as a minimum value. The rose diagram of the long shape axis of the metal grains shows a weak shape preferred orientation (SPO) running NE–SW relative to the orientation of the EBSD map (Figure 10b). This is consistent with the relatively strong 3-D SPO observed in XCT data (Figure 7). However, there is no crystallographic preferred orientation (CPO) with metal grains, which instead exhibit a random orientation evidenced by their lower hemisphere pole figures (Figure 10c) as well as an m-index of 0.023 ± 0.0005 and a j-index of 1.50 ± 0.03.
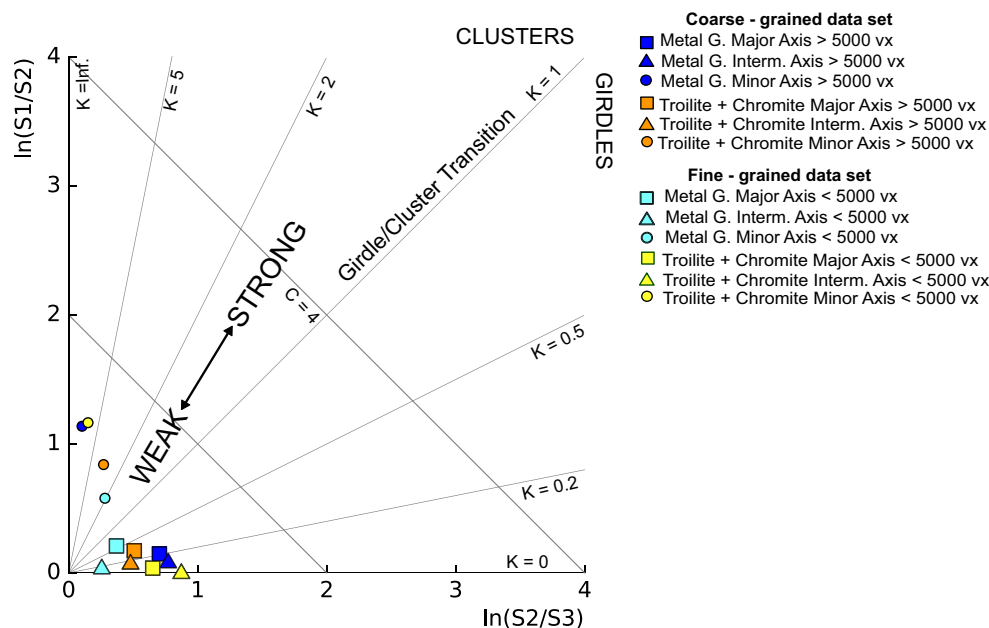
FIGURE 9. Eigenvalue ratio graph for the different phase groups and grain size classes, following the approach of Woodcock and Naylor (1983). The major and intermediate axes of both phase groups and grain size classes define a girdle distribution, whereas the minor axes of both phase groups and grain size classes define a cluster distribution.

The m-index can vary from 0 (random) to 1 (single crystal), whereas the j-index varies from 1 (random) to infinity (single crystal). Thus, our data are indicative of a random crystallographic texture (Figure 10c, Table S2). The metal grains are highly deformed with an average and median mean orientation spread (typically referred to as grain orientation spread—GOS, Brewer et al., 2009) of 5.3° and 4.74°, respectively, and an average and median maximum orientation spread (typically referred to as MOS, Brewer et al., 2009) of 14.7° and 12.5°, respectively.

Troilite is likely underestimated in the large-area EBSD data relative to the XCT data, as troilite grains are porous and microcrystalline, containing many fine crystals that were smaller than the step size of the large-area EBSD map (Figure 10a). This microcrystalline texture results in mixed patterns and poor indexing (Figure 10a). High-resolution EBSD maps of the troilite grains reveal that they are porous microcrystalline aggregates with random orientations, minimal to no internal deformation, and 120° triple junction grain boundaries (Figure 12a–h). The GROD angle maps show that some troilite microcrystallites have high internal deformation (Figure 12d,h). However, as the coloration is relatively uniform within what appear to be discrete grains, this is likely not due to high internal crystal plastic deformation but instead due to the presence of low angle boundaries <10° indicative of subgrains (Figure 12d,h). Due to the microcrystalline nature of the troilite grains, SPO and CPO could not be determined for this phase from the large-area EBSD maps.

In the large-area EBSD maps, 5684 olivine grains >50 pixels were detected (Figure 11d, Table S3). One point per crystallite stereographic projection crystallographic orientation data of olivine revealed a random CPO (Figure 11d). This interpretation is also supported by calculations of the m-index of 0.0024 ± 0.0005, the j-index of 1.25 ± 0.025, and Vollmer diagrams that also reveal a random crystallographic texture (Figure 11, Table S2). The olivine grains are weakly deformed with an average and median mean orientation spread (typically referred to as grain orientation spread—GOS; Brewer et al., 2009) of 1.74° and 1.35°, respectively, and an average and median maximum orientation spread (typically referred to as MOS; Brewer et al., 2009) of 5.89° and 4.79°, respectively (Figure 11b).

From the GOS data, we calculate the skewness value (Sk; previously known as, inferred annealing parameter as high skewness can be indicative of recovery of intracrystalline deformation during annealing; however, there can be other causes, hence the name change to describe the measurement not the interpretation, Ruzicka & Hugo, 2018; Ruzicka et al., 2024) of mean $GOS_{n>50px}$/median $GOS_{n>50px}$ (where $n > 50px$ is the number of grains where the number of pixels within a grain is above 50: This is distinct from that used in Ruzicka & Hugo, 2018; Ruzicka et al., 2024 which used circle equivalent diameters of $>50\,\mu m$) of 1.30 (Figure 13, Table S4). Values of Sk >1 indicate positive skewness (high proportion of low-GOS grains but the presence of some high-GOS grains), and Sk <1 indicates negative skewness.
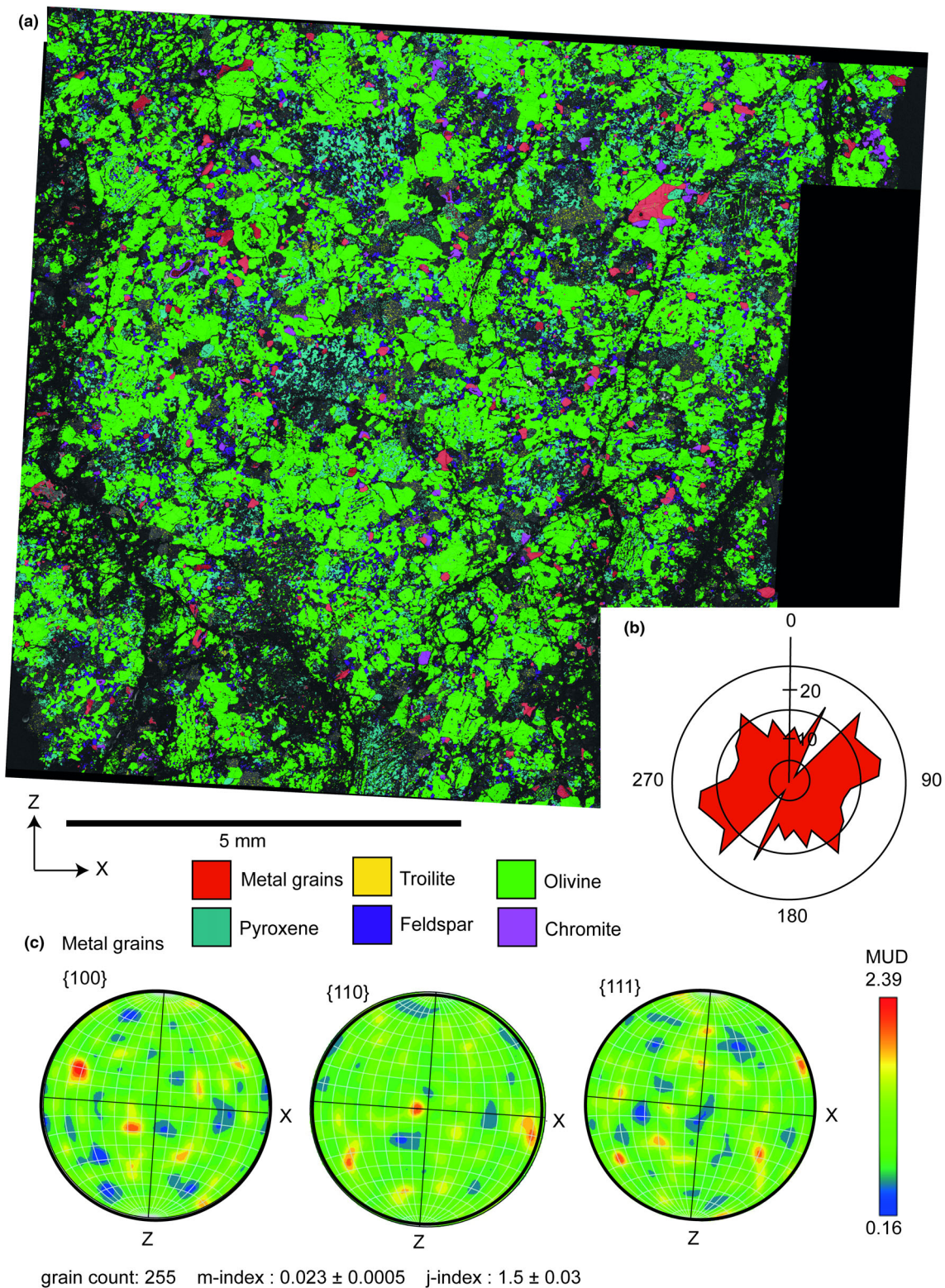
FIGURE 10. EBSD data from Ozerki rotated into the same reference frame as the XCT data. (a) An EBSD phase map showing the distribution of minerals within the Ozerki meteorite. (b) A rose diagram of the long shape axis orientations of metal grains revealing a weak SPO. (c) Contoured and smoothed lower hemisphere pole figures of the main crystallographic axes {100}, {110}, and {111} of metal grains revealing a random CPO, as well as the m-index and j-index texture metrics.

We also calculated the misorientation rotation parameter $R_{2-10°}$ ratio (previously known as the inferred temperature parameter, as it could be linked to the ambient temperature during deformation; however, there can be other causes, hence the name change to describe the measurement not the interpretation (Ruzicka & Hugo, 2018)), by measuring the relative proportion of the 2–10° crystal rotation axes of olivine, determined by taking the MUD value at the <100>, <010>, and <001> positions (far corners) on the crystal rotation axis diagram (Figure 11b; <100>:<010>:<001> was 1.73:1.13:0.83) and normalizing each principal crystallographic axis' MUD relative to the total MUD of all axes: <100>:<010>:<001> was 0.47:0.31:0.22 using a 25° halfwidth. The final part of the calculation is then to sum the values for <010> and <001> together as they generally reflect the rotation axis/slip systems that activate at lower ambient temperatures, following the approach of Ruzicka and Hugo (2018). This corresponds to a misorientation rotation parameter R_{2-10} value of 0.53 (Ruzicka & Hugo, 2018; Hugo et al., 2020; Figure 13). The strong cluster of data around the <100> direction as well as the Weighted Burgers Vector (WBV) suggest that the (010)[001] slip system is predominantly accommodating deformation and strain in olivine (Figure 11b,d). The GROD angle map shows that crystal plastic deformation within the meteorite is heterogeneously distributed with elongate areas of intense >5° (colored green–yellow–red) internal deformation that correlates with fractures in the meteorite (Figure 11a). This intense deformation contrasts with areas of little to no internal deformation (<2°) located in between these highly deformed fractured zones (Figure 11a). Subsets were extracted from highly deformed zones and weakly deformed zones, and we then calculated the misorientation rotation parameter R_{2-10} values of 0.55 and 0.49, respectively, and Sk of 1.15 and 1.24, respectively, for each zone. In addition, some chondrules exhibit high internal misorientations even when within the weakly deformed zone (Figures 11a and 12e–h).
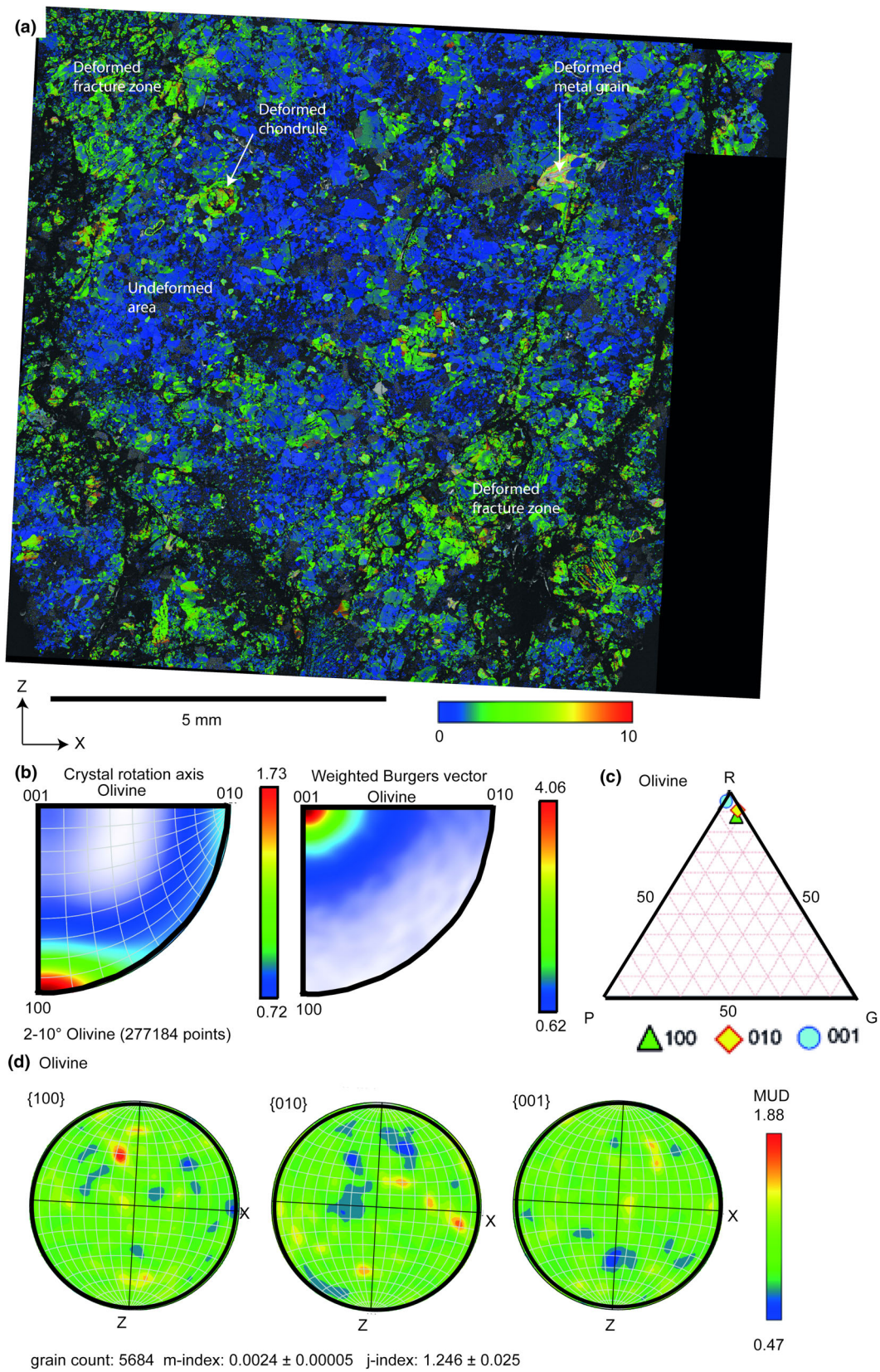
DISCUSSION

The XCT technique has been used previously to detect 3-D petrofabrics in meteorites (Almeida, 2018; Friedrich et al., 2008; Friedrich & Rivers, 2013; Hanna & Ketcham, 2017; Krzesińska, 2011; Martell et al., 2022).

Specifically, it has been used to explore metal and sulfide grain textures and fabrics which have been used to infer shock stage and degree of deformation (Benedix et al., 2008; Friedrich et al., 2008; Friedrich & Rivers, 2013; Hanna & Ketcham, 2017). Similarly, EBSD has been used on meteorites to define new shock classification systems, assess the degree of deformation, and annealing to determine whether the ordinary chondrite was impacted while still hot or cool (Hugo et al., 2020; Ruzicka & Hugo, 2018). EBSD is also a powerful tool for textural analysis, especially where it can be assumed that crystallography and shape are linked (Daly, Lee, et al., 2019; Daly, Piazolo, et al., 2019; Forman et al., 2017, 2019; Griffin, Daly, Keller, 2022; Griffin, Daly, Piazolo, 2022). As such, both techniques are useful tools to determine shock deformation in chondrite meteorites but are rarely used together. Here, we combine both techniques to explore the deformation and shock history of the Ozerki L6 ordinary chondrite.

3-D–2-D Texture Comparison for a Correlative Approach

Our XCT data show that the Fe-metal and troilite + chromite grains in Ozerki have a moderate foliation petrofabric (Figures 7–9). However, this fabric, while present, is much weaker in the 2-D SPO data collected by SEM-EBSD analysis (Figure 10b). It is likely that this discrepancy is caused by the cut of the Ozerki section and the plane on which the SEM analysis was undertaken. When the foliation plane detected in XCT data is rotated to be in the same spatial reference plane as the SEM images, it reveals that the foliation plane is approximately parallel to the plane of the sample surface. This would result in the long shape axis directions of Fe-metal being oriented in the plane of the section and, therefore, would appear nearly evenly distributed around the plane of the section. The near-parallel orientation of the sample surface and foliation fabric would result in the Fe-metal grain shape orientations presenting a much weaker fabric in the 2-D EBSD data set than in the 3-D XCT data set. This reinforces the importance of doing correlative 2-D and 3-D work when characterizing petrofabrics and textures within geological and extraterrestrial materials (Ebel et al., 2008; Hertz et al., 2003; Martell et al., 2022; Ruzicka et al., 2015a; Tait et al., 2014). 3-D fabric analysis is essential to determine true foliation and

FIGURE 11. EBSD data from Ozerki rotated into the same reference frame as the XCT data. (a) A GROD angle map showing the internal deformation of olivine and metal grains relative to the average orientation of each grain. (b) A crystal rotation axis plot and Weighted Burgers Vector plot showing that the dominant slip system that is accommodating strain in olivine across the whole section is the (010)[001] slip system. (c) Vollmer plot of the main crystallographic axes 100, 010, and 001 of olivine showing also a random distribution ("P" = point, "G" = girdle, "R" = random). (d) Contoured and smoothed lower hemisphere pole figures of the main crystallographic axes {100}, {010} and {001} of olivine revealing a random CPO as well as the m-index and j-index texture metrics.

(a) Deformed fracture zone; Deformed chondrule; Deformed metal grain; Undeformed area; Deformed fracture zone

Z; X; 5 mm; 0 10

(b) Crystal rotation axis Olivine; Weighted Burgers vector Olivine; 2-10° Olivine (277184 points)

(c) Olivine; 100; 010; 001

(d) Olivine; {100}; {010}; {001}; MUD 1.88; 0.47; grain count: 5684 m-index: 0.0024 ± 0.00005 j-index: 1.246 ± 0.025
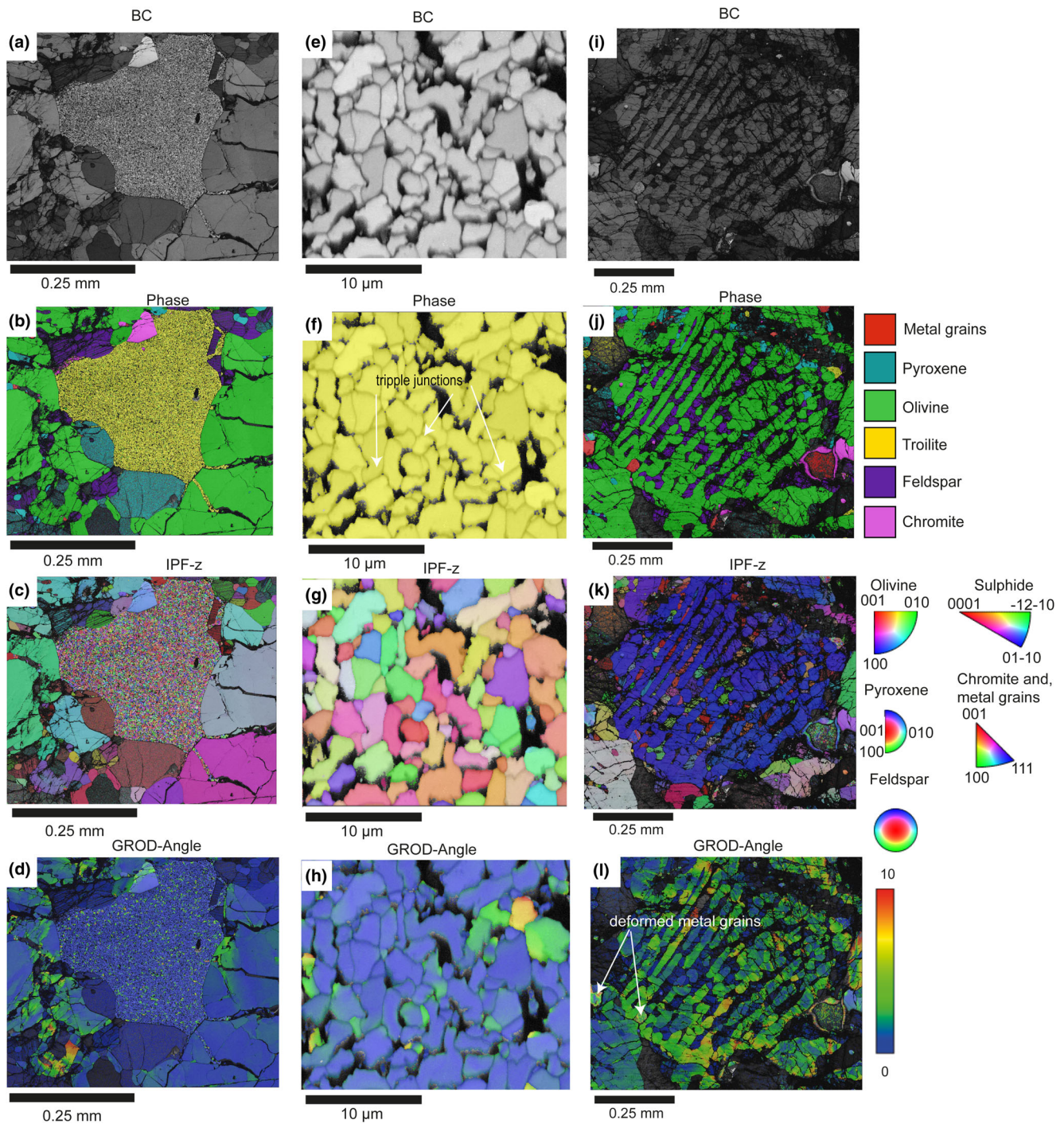
FIGURE 12. EBSD maps showing sulfide and chondrule morphology. (A–D) EBSD band contrast (BC), phase map, inverse pole figure (IPF)-Z map, and GROD-angle map, respectively, showing a nanocrystalline and porous sulfide grain that is surrounded by olivine, pyroxene, and feldspar. The sulfide phase is being injected into surrounding mineralogy along fractures. (E–H) EBSD BC, phase map, IPF-Z map, and GROD-angle map, respectively, showing the nanocrystalline and porous sulfide grain showing pores and 120° triple junctions. (I–L) EBSD BC, phase map, IPF-Z map, and GROD-angle map, respectively, showing a highly deformed barred olivine chondrule with coarse crystals of feldspar in the mesostasis.

lineation fabrics unambiguously from the cut of the section and could be used to better interpret physical processes (Almeida, 2018; Friedrich et al., 2008; Friedrich & Rivers, 2013; Hanna & Ketcham, 2017; Krzesińska, 2011; Martell et al., 2022) and inform sectioning.
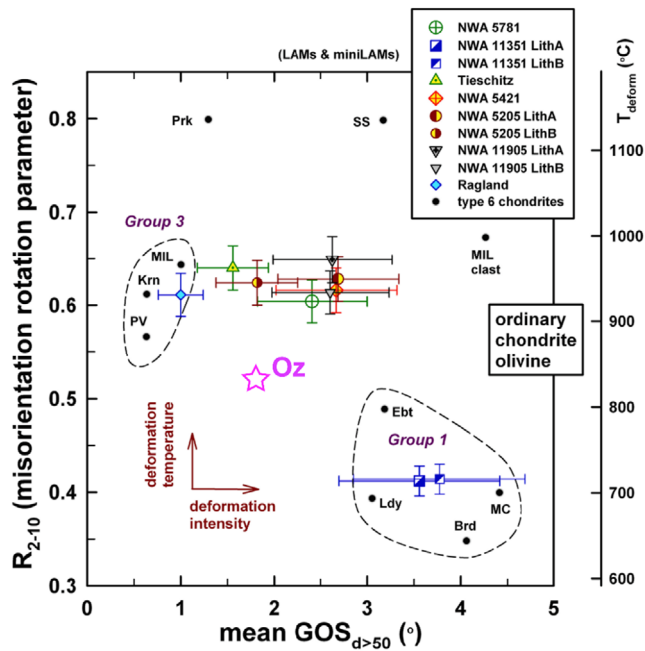
FIGURE 13. R2-10 versus mean $GOS_n > 50px$ of olivine in Ozerki (pink) relative to other ordinary chondrites. Additional ordinary chondrite data from Ruzicka and Hugo (2018) and Ruzicka et al. (2024) and figure after Ruzicka et al. (2024).

Comparison Between Ozerki Mineralogy from XCT, EBSD Data, and the Literature

Visually, our XCT and SEM-EBSD analyses reveal that the Ozerki L6 meteorite is composed of a silicate matrix, rich in olivine grains and chondrules. The brightest phases in the XCT data are the Fe-metal grains and the troilite + chromite grains, which account for ~3.1 vol% and ~5.4 vol%, respectively. While not directly comparable due to possible density variations within metal grains, our XCT data are broadly consistent with the overall mineralogy and relative abundances derived from XRD that has been reported by Maksimova et al. (2020) who stated that Ozerki contains 4.5 wt% troilite, 1.5 wt% chromite, and 2.5 wt% Fe-metal. Maksimova et al. (2020) described Ozerki as being characterized by the presence of Fe-Ni-Co alloy grains, troilite, and chromite inclusions in a silicate matrix, composed of olivine and pyroxenes. Maksimova et al. (2020) also observed that the troilite inclusions are quite porous, consistent with our EBSD observations (Figure 12a–h). Similarly, our EBSD data also reported comparable values for the Fe-Ni-bearing metals (3.5 area%) and chromite (1.8 area%) to that of Maksimova et al. (2020). However, our troilite abundance (0.9 area%) was largely underestimated relative to Maksimova et al. (2020) due to the EBSD step size for the large-area map being greater than many of the microcrystalline troilite grains (Figure 10a).

Implications of the Observed Petrofabrics in Ozerki's Metal, Sulfide, and Chromite Grains

Our XCT data show a shape preferred orientation of metal and troilite + chromite phases (Figures 7–9, 10b). 3-D XCT shows that the strength parameter (C) and shape factor (K) for the major and intermediate axes of metals and sulfide grains reveal weak to moderate orientations and very low (<1) K values, indicative of a foliation and girdle distribution (Figures 7–9). In contrast, values for the minor axis indicate a cluster distribution that is indicative of a lineation (Figures 7–9). It should be noted that, while our data plot in areas of the Vollmer graph that are traditionally associated with weak and moderate fabric strengths, these are usually derived from metallurgical literature where very strong fabric alignments are produced. For geological materials and extraterrestrial samples, even weak to moderate fabrics in this plot should be considered quite strong in nature (Daly, Piazolo, et al., 2019; Griffin, Daly, Keller, 2022; Griffin, Daly, Piazolo, 2022). The girdle maxima present in the major and intermediate axes of the metal and troilite + chromite grains, alongside the point maxima in the minor axis (Figure 7) is typical of a moderate shape fabric defining a foliation (Paterson et al., 1998). The consistency of fabric and shape indicates that both phases, regardless of grain size, were likely deformed in a similar manner by the same process. Preferred shape orientation foliations of metal and sulfide grains have been described before in ordinary and carbonaceous chondrites (Benedix et al., 2008; Friedrich et al., 2008; Friedrich & Rivers, 2013; Gattacceca et al., 2005; Hanna & Ketcham, 2017; Krzesińska, 2011). The alignment of grains is interpreted to be formed by hypervelocity impact in a pure shear flattening regime (Benedix et al., 2008; Friedrich et al., 2008; Friedrich & Rivers, 2013; Gattacceca et al., 2005; Hanna & Ketcham, 2017; Krzesińska, 2011). The orientation of metal and sulfide grains within ordinary chondrites is known to produce a fabric within increasing shock pressure above 15 GPa but has also been reported in S1 chondrites <5 GPa (Friedrich et al., 2008). The moderate fabric strength and C metrics calculated from metal and sulfide grains for the major axis (0.84 and 0.75, respectively) indicate that Ozerki was highly shocked (Figure 7a,c) (Friedrich et al., 2008) consistent with the classification of Ozerki as a S4/5 based on planar fractures in olivine and shock melt veins (Gattacceca et al., 2020). The fabric strength is correlated with the shock stage, with higher shock stages exhibiting higher fabric strengths (Friedrich et al., 2008; Hanna & Ketcham, 2017). While our data are largely consistent with this interpretation, a few additional nuances can be extracted.

The shape of the fine-grained data set shows that, while most of the data in metal and sulfide grains have

a random shape, there is a preference toward prolate shapes (Figure 6). Prolate grain shapes are typically interpreted as being generated by constrictional strain. However, the coarser grained data set shows no predominant preferred shape and can range from prolate to oblate (Figure 6). The mineral fabrics defined by the shape of the grains are oriented in a foliation fabric consistent with pure shear, flattening strain. This girdle fabric is consistent with impact as interpreted previously (Benedix et al., 2008; Friedrich et al., 2008; Friedrich & Rivers, 2013; Gattacceca et al., 2005; Hanna & Ketcham, 2017; Krzesińska, 2011). The prolate shapes of the fine-grained data sets could either be caused by impact compaction with an oblique component resulting in simple shear and constrictional flow, or this could be the result of pure shear flattening of originally irregularly shaped objects. Constrictional flow results in the production of a lineation fabric, and so we would expect to see a trend from the coarse-grained data set to the fine-grained data set of an increased lineation fabric strength. This is not observed in the data, and the fine-grained data set becomes systematically weaker in strength (Figure 8). Therefore, we interpret that metal and sulfide grains were originally irregular shapes with a tendency toward prolate shapes in the fine-grained data set.

It is interesting to note that the data set of smaller grains of metals and sulfides shows a lower fabric strength relative to the coarser grained data set and have a slightly shifted lineation orientation in the minor axis (Figures 7–9). This could indicate that smaller grains are more resistant to deformation during impacts and/or are more affected by local heterogeneities. This resistance to deformation is contrary to other observations where the finer grained materials are preferentially affected and can even be reset during impact processing (Bland et al., 2014; Forman et al., 2017, 2019). Indeed, it is likely that the slight offset of minor axis lineations orientation between coarse- and fine-grained phases could be explained by a later second impact at a slightly different orientation reorienting finer grained materials preferentially (Forman et al., 2017, 2019). However, this would not explain the lower fabric strength, and thus, this contradiction could be reconciled by accounting for the petrologic context of the fine-grained metal/sulfide population. For example, many of the smaller metal and sulfide grains are contained within harder silicates such as olivine which could protect the mineral and preserve the metal/sulfide grain's original shape and orientation reducing the fabric strength. Conversely, the larger metal and sulfide grains are predominantly hosted within the matrix and do not have such protection and so would deform more easily and flow into open pore space.

Crystallography of Metal Grains is Decoupled From Shape

The EBSD data, while compromised somewhat by the cut of the section, still show the preferred SPO of the metal grains (Figure 10b). However, the crystallographic orientations and quantitative textural analysis of the metal grains do not show a preferred alignment and instead show a random texture (Figure 10c). This indicates that the crystallography and shape have been decoupled from each other during deformation. EBSD data show that the metal grains are also highly deformed with >10° internal misorientation and are evidence of severe internal deformation (Figures 11a and 12h). Therefore, the decoupling of crystallography and shape is consistent with the metal grain reorientation during deformation being caused by internal crystal plastic deformation of the metal rather than a physical rotation of the grain. The microstructures of these metal grains with sweeping crystal plastic deformation rather than discrete low angle boundaries also suggest minimal recovery occurred post deformation, and so these samples likely experienced minimal annealing post shock (Ruzicka, Brown, et al., 2015; Ruzicka & Hugo, 2018). It also suggests that these metals were deformed into a shape preferred alignment in the solid state without melting.

Preferential Deformation of Chondrules

We observe in our EBSD data that chondrules in Ozerki appear to be preferentially deformed relative to the surrounding matrix (Figures 11 and 12h). These chondrules can be highly deformed even within regions of the meteorite where the matrix is minimally deformed (Figures 11 and 12h). Numerical simulations of impacts into a bimodal media comprising solid spherical objects (chondrules) in a porous fine-grained suspension (matrix) suggest that, during impact compaction, the porous fine-grained material will experience higher temperatures and pressures than the solid chondrule objects (Bland et al., 2014). Evidence for this has also been observed in the Allende meteorite, where matrix grains show elevated internal misorientation relative to chondrules that are relatively undeformed (Forman et al., 2016). However, in Ozerki, we observe the opposite with chondrules exhibiting elevated internal misorientation relative to the surrounding undeformed matrix. This is partially explained by Ozerki being an L6 chondrite, which has therefore experienced substantial post-accretion heating due to the decay of short-lived radionuclides (Dodd, 1969). This heating would both equilibrate olivine Fo-Fa compositions and result in grain coarsening in the matrix and reduce matrix porosity (Dodd, 1969; Weisberg

et al., 2006). This thermal processing would also erase any pre-existing microstructures derived from impact compaction or accretion (Ruzicka & Hugo, 2018). It is possible that the chondrules are preserving microstructures from chondrule formation; this could be the case for the barred olivine chondrules, which formed by supercooling, and the rapid growth would result in defects. However, chondrules would also be subject to this recrystallization/annealing and grain deformation recovery process, also resulting in the erasure of microstructures caused by chondrule formation resulting in a series of low and high angle boundaries which is not observed in the chondrules in Ozerki. Instead, Ozerki chondrules show more crystal plastic deformation (Figure 12l). We speculate that the chondrules in Ozerki may exhibit more deformation than the surrounding matrix via constructive interference of the shock wave that generated the deformation microstructures and metal/sulfide petrofabrics. In this scenario, impact into a solid media with embedded spherical chondrules results in a deviation of the passage of the shock wave generating locally elevated shock pressures, or alternatively, chondrules act as a point of weakness within the main body of the chondrite. Either scenario would result in an increase in deformation within the chondrule relative to the surrounding matrix.

Implications from EBSD Temperature and Annealing Parameters

The EBSD relative deformation temperature ($R_{2\text{-}10°}$) and skewness parameter (mean $GOS_{n>50px}$/median $GOS_{n>50px}$) indicate that Ozerki is related to neither group 1 nor group 3 ordinary chondrites as described by Ruzicka and Hugo (2018) or Ruzicka et al. (2024). Group one ordinary chondrites have experienced high shock at low ambient temperatures (Figure 13) and group 3 ordinary chondrites have experienced low shock at high deformation temperatures. Ozerki spans the gap between these two groups, suggesting moderate deformation and moderate temperatures, reducing the gap between these groups (Figure 13). These EBSD results indicate that, while Ozerki was also highly shocked like group one ordinary chondrites at relatively low temperatures, its ambient temperature was slightly higher than other group one ordinary chondrites (Ruzicka & Hugo, 2018). Another possibility is that Ozerki experienced partial re-setting from a primary chondrite belonging to group three. Our chondrite may come from slightly less-shocked affected areas, experiencing only partial re-set. This was also observed by Ruzicka et al. (2024) for shock stage S4, like the one we have. In any case, these results hint that a spectrum may exist between group one and group three meteorites outlined in Ruzicka et al. (2024). More

ordinary chondrites across a range of petrological types and shock classifications should be explored in this way.

Ozerki is classified as S4-5 (based on observations of undulose extinction, irregular and planar fractures in olivine and opaque shock veins; Gattacceca et al., 2020). However, Ruzicka et al. (2024) show that there is a relationship between mean $GOS_{d>50µm}$ and weighted shock stage (Jamsja & Ruzicka, 2010). Ozerki's mean $GOS_{d>50px}$ is 1.66 which would indicate a weighted shock stage of ~S2. Shock metamorphism is known to be highly heterogeneously distributed through rocks, particularly those with anisotropy (Bland et al., 2014; Huffman & Reimold, 1996). This heterogeneity is also evident in Ozerki as our sample contained no shock melt veins that have been reported in other Ozerki samples (Gattacceca et al., 2020). The GROD-angle EBSD maps also support the inference that shock effects are heterogeneously distributed as the Ozerki meteorite contains elongate fracture zones that extend across the sample that are separated by "islands" of low internal misorientation (Figure 11). If elevated post shock temperatures resulted in annealing, then we would expect to see a higher skewness parameter (mean $GOS_{n>50px}$/median $GOS_{n>50px}$) in the high deformation zones. However, when the high and low deformation zones are considered separately, it is the areas with low overall internal misorientation that exhibit the highest skewness parameter. This suggests that the meteorite was shocked at elevated ambient temperatures and may have permitted some recovery of the microstructure as proposed by Ruzicka and Hugo (2018). It has been suggested that the skewness ratio of small grains 5–15 µm circle equivalent diameter to coarse grains >50 µm circle equivalent diameter can be used to robustly evaluate and interpret whether this resetting of the microstructure is due to annealing processes (Ruzicka et al., 2024). However, we cannot reliably calculate this as our step size of 4 µm means that grains that are 5–15 µm circle equivalent diameter in size will only be sampled by 2–22 pixels which are insufficient data to reliably extract GOS values. Regardless, our data show at least some resetting of the primary accretionary microstructure.

Sulfide Textures

The sulfides in Ozerki are microcrystalline aggregates with a porous texture. This texture has been reported previously (Rubin, 2002; Ruzicka, Brown et al., 2015; Ruzicka, Hugo, et al., 2015; Schmitt, 2000). Our EBSD data show that these microcrystals are undeformed and randomly oriented, and grains meet at 120° triple junctions with predominantly high-angle boundaries. Additionally, the sulfide grains also penetrate neighboring minerals along fractures. This texture could

be explained by annealing, recrystallization, or solidification with abundant nucleation sites (Rubin, 2002; Ruzicka, Brown et al., 2015; Ruzicka, Hugo, et al., 2015; Schmitt, 2000). 120° triple junctions and no internal misorientation are consistent with annealing textures in line with previous interpretations of these minerals (Rubin, 2002; Ruzicka, Brown et al., 2015; Ruzicka, Hugo, et al., 2015; Schmitt, 2000). However, the predominance of high-angle boundaries versus low-angle boundaries is not consistent with annealing. Injection of sulfide into fractures suggests that the mineral assemblage was once molten consistent with solidification with abundant nucleation sites. However, this would not immediately explain the porous nature of the assemblage. The porous texture is suggestive of recrystallization, as is supported by the random orientation sub-grains, 120° triple junctions, and a dominance of high-angle boundaries. It should be noted that, in both recrystallization or solidification, pores could be produced by the rapid formation and loss of an S_2 gas (as seen previously by Andronikov et al., 2015; Benedix et al., 2008; Ruzicka et al., 2020; Zhang et al., 2013). While we cannot rule out solidification, our data lead toward the interpretation that these sulfide grains formed by recrystallization during high shock, as at high pressure, sulfide melts and recrystallizes, and this process would also lead to the moderate SPO fabric observed in the XCT data.

We propose that sulfide grains experienced melting during impact, resulting in the alignment of sulfide melt in a foliation fabric and injection of melt into the neighboring matrix. This was then followed by a period of cooling and recrystallization involving the release of an S-rich gas to produce the porous texture observed (Ruzicka, Hugo, et al., 2015; Schmitt, 2000). Given these textures are dependent on temperature (Dai et al., 2001; Daly et al., 2017), these microstructures could be used as a coarse thermometer and the relative lack of crystal microstructure recovery in metal and olivine, combined with evidence of recrystallization in the sulfides (Figure 12a–h), if calibrated, could be used to make a more precise interpretation of post-shock temperatures.

CONCLUSIONS

Correlative XCT-EBSD has been combined to compare their relative efficacies at characterizing the petrofabrics and shock deformation microstructures of ordinary chondrites. We find that 2-D analysis from SEM-EBSD can be heavily influenced by the cut of the section, which can obscure the true 2-D fabric strength. We reaffirm that 3-D microanalysis is required alongside classical 2-D texture analysis and 3-D measurements are an ideal first step to inform further sampling of the

material relative to known texture orientations. Moreover, 3-D microanalysis provides a more complete quantitative view of mineral abundance. However, minor challenges arise when two phases have similar X-ray attenuations and require correlation with SEM-EBSD. Therefore, the two techniques are highly complementary.

In the case of the Ozerki meteorite, we show that both metal and sulfide grains were deformed in the same impact event. EBSD-derived deformation, skewness, and relative deformation temperature parameters show that the parent body of Ozerki likely has not had its primary accretionary texture completely overprinted by subsequent shock, which means that it must have been deformed while it still retained some of its primordial heat and suggests that this impact and fabric must have been established within the first 100 My of solar system history. Ozerki's deformation microstructure parameters occupy a gap between group one and group three ordinary chondrites proposed by Ruzicka and Hugo (2018) and Ruzicka et al. (2024) and hint that a spectrum may exist between low shock ordinary chondrites, deformed while the asteroid was hot, and high shock ordinary chondrites, deformed while the asteroid was cold. Further work on ordinary chondrites across all shock classifications might fill in the gaps between these two groups, which would suggest large impacts into chondritic parent bodies were common during the early solar system over the lifetime of heat generation by cosmogenic radionuclides.

Data Availability Statement—The data that support the findings of this study are available from the corresponding author upon reasonable request.

Editorial Handling—Dr. Jull A. J. Timothy

REFERENCES

Almeida, N. V. 2018. Three-Dimensional Features of Chondritic Meteorites: Applying Micro-Computed Tomography to Extraterrestrial Material PhD thesis. University of London, Birkbeck.

Andronikov, A. V., Andronikova, I. E., and Hill, D. H. 2015. Impact History of the Chelyabinsk Meteorite: Electron Microprobe and LA-ICP-MS Study of Sulfides and Metals. *Planetary and Space Science* 118: 54–78.

Arganda-Carreras, I., Kaynig, V., Rueden, C., Eliceiri, K. W., Schindelin, J., Cardona, A., and Sebastian Seung, H. 2017. Trainable Weka Segmentation: A Machine Learning Tool for Microscopy Pixel Classification. *Bioinformatics* 33: 2424–26.

Baker, D. R., Mancini, L., Polacci, M., Higgins, M. D., Gualda, G., Hill, R., and Rivers, M. 2012. An Introduction to the Application of X-Ray Microtomography to the Three-Dimensional Study of Igneous Rocks. *Lithos* 148: 262–276. https://doi.org/10.1016/j.lithos.2012.06.008.

Benedix, G., Ketcham, R., Wilson, L., McCoy, T. J., Bogard, D., Garrison, D., Herzog, G. F., Xue, S., Klein, J., and Middleton, R. 2008. The Formation and Chronology of the PAT 91501 Impact-Melt L Chondrite with Vesicle–Metal–Sulfide Assemblages. *Geochimica et Cosmochimica Acta* 72: 2417–28. https://doi.org/10.1016/j.gca.2008.02.010.

Bland, P. A., Collins, G., Davison, T., Abreu, N., Ciesla, F., Muxworthy, A., and Moore, J. 2014. Pressure–Temperature Evolution of Primordial Solar System Solids during Impact-Induced Compaction. *Nature Communications* 5: 1–13.

Brewer, L. N., Field, D. P., and Merriman, C. C. 2009. Mapping and Assessing Plastic Deformation Using EBSD. In *Electron Backscatter Diffraction in Materials Science*, 251–262. Boston, MA: Springer US. https://doi.org/10.1007/978-0-387-88136-2_18.

Dai, Z., Sun, S., and Wang, Z. 2001. Phase Transformation, Coalescence, and Twinning of Monodisperse FePt Nanocrystals. *Nano Letters* 1: 443–47. https://doi.org/10.1021/nl0100421.

Daly, L., Bland, P. A., Dyl, K. A., Forman, L. V., Saxey, D. W., Reddy, S. M., Fougerouse, D., et al. 2017. Crystallography of Refractory Metal Nuggets in Carbonaceous Chondrites: A Transmission Kikuchi Diffraction Approach. *Geochimica et Cosmochimica Acta* 216: 42–60. https://doi.org/10.1016/j.gca.2017.03.037.

Daly, L., Lee, M. R., Piazolo, S., Griffin, S., Bazargan, M., Campanale, F., Chung, P., et al. 2019. Boom Boom Pow: Shock-Facilitated Aqueous Alteration and Evidence for Two Shock Events in the Martian Nakhlite Meteorites. *Science Advances* 5: eaaw5549. https://doi.org/10.1126/sciadv.aaw5549.

Daly, L., Piazolo, S., Lee, M. R., Griffin, S., Chung, P., Campanale, F., Cohen, B. E., et al. 2019. Understanding the Emplacement of Martian Volcanic Rocks Using Petrofabrics of the Nakhlite Meteorites. *Earth and Planetary Science Letters* 520: 220–230. https://doi.org/10.1016/j.epsl.2019.05.050.

Devillepoix, H. A. R., Cupák, M., Bland, P., Sansom, E., Towner, M., Howie, R. M., Hartig, B. A. D., et al. 2020. A Global Fireball Observatory. *Planetary and Space Science* 191: 105036. https://doi.org/10.1016/j.pss.2020.105036.

Dmitriev, V., Lupovka, V., and Gritsevich, M. 2015. Orbit Determination Based on Meteor Observations Using Numerical Integration of Equations of Motion. *Planetary and Space Science* 117: 223–235. https://doi.org/10.1016/j.pss.2015.06.015.

Dodd, R. 1969. Metamorphism of the Ordinary Chondrites: A Review. *Geochimica et Cosmochimica Acta* 33: 161–203.

Ebel, D. S., Weisberg, M. K., Hertz, J., and Campbell, A. J. 2008. Shape, Metal Abundance, Chemistry, and Origin of Chondrules in the Renazzo (CR) Chondrite. *Meteoritics & Planetary Science* 43: 1725–40. https://doi.org/10.1111/j.1945-5100.2008.tb00639.x.

Forman, L. V., Bland, P. A., Timms, N. E., Daly, L., Benedix, G. K., Trimby, P. W., Collins, G. S., and Davison, T. M. 2017. Defining the Mechanism for Compaction of the CV Chondrite Parent Body. *Geology* 45: 559–562. https://doi.org/10.1130/G38864.1.

Forman, L., Bland, P. A., Timms, N. E., Collins, G., Davison, T., Ciesla, F., Benedix, G. K., et al. 2016. Hidden Secrets of Deformation: Impact-Induced Compaction within a CV Chondrite. *Earth and Planetary Science Letters* 452: 133–145. https://doi.org/10.1016/j.epsl.2016.07.050.

Forman, L., Timms, N., Bland, P., Daly, L., Benedix, G., and Trimby, P. 2019. A Morphologic and Crystallographic Comparison of CV Chondrite Matrices. *Meteoritics & Planetary Science* 54: 2633–51. https://doi.org/10.1111/maps.13380.

Friedrich, J. M., and Rivers, M. L. 2013. Three-Dimensional Imaging of Ordinary Chondrite Microporosity at 2.6 µm Resolution. *Geochimica et Cosmochimica Acta* 116: 63–70.

Friedrich, J. M., Wignarajah, D. P., Chaudhary, S., Rivers, M. L., Nehru, C., and Ebel, D. S. 2008. Three-Dimensional Petrography of Metal Phases in Equilibrated L Chondrites—Effects of Shock Loading and Dynamic Compaction. *Earth and Planetary Science Letters* 275: 172–180. https://doi.org/10.1016/j.epsl.2008.08.024.

Gattacceca, J., Mccubbin, F. M., Bouvier, A., and Grossman, J. 2020. The Meteoritical Bulletin, No. 107. *Meteoritics & Planetary Science* 55: 460–62.

Gattacceca, J., Rochette, P., Denise, M., Consolmagno, G., and Folco, L. 2005. An Impact Origin for the Foliation of Chondrites. *Earth and Planetary Science Letters* 234: 351–368.

Goudy, S. P., Telus, M., and Chapman, B. 2023. Evidence for Multiple Early Impacts on the H Chondrite Parent Body from Electron Backscatter Diffraction Analysis. *Meteoritics & Planetary Science* 58: 501–515. https://doi.org/10.1111/maps.13969.

Griffin, S., Daly, L., Keller, T., Piazolo, S., Forman, L. V., Lee, M. R., Baumgartner, R. J., et al. 2022. Constraints on the Emplacement of Martian Nakhlite Igneous Rocks and their Source Volcano from Advanced Micro-Petrofabric Analysis. *Journal of Geophysical Research: Planets* 127: e2021JE007080. https://doi.org/10.1029/2021JE007080.

Griffin, S., Daly, L., Piazolo, S., Forman, L. V., Cohen, B. E., Lee, M. R., Trimby, P. W., Baumgartner, R. J., Benedix, G. K., and Hoefnagels, B. 2022. Can the Magmatic Conditions of the Martian Nakhlites be Discerned Via Investigation of Clinopyroxene and Olivine Intracrystalline Misorientations? *Journal of Geophysical Research: Planets* 127: e2021JE007082. https://doi.org/10.1029/2021JE007082.

Gritsevich, M. 2009. Determination of Parameters of Meteor Bodies Based on Flight Observational Data. *Advances in*

Space Research 44: 323–334. https://doi.org/10.1016/j.asr. 2009.03.030.

Gritsevich, M. I. 2007. Approximation of the Observed Motion of Bolides by the Analytical Solution of the Equations of Meteor Physics. *Solar System Research* 41: 509–514. https://doi.org/10.1134/S003809460706007X.

Gritsevich, M. I., Stulov, V. P., and Turchak, L. I. 2012. Consequences of Collisions of Natural Cosmic Bodies with the Earth's Atmosphere and Surface. *Cosmic Research* 50: 56–64. https://doi.org/10.1134/S0010952512010017.

Gritsevich, M., Lyytinen, E., Kohout, T., Moilanen, J., Midtskogen, S., Kruglikov, N. A., Ischenko, A., et al. 2014. Analysis of the Bright Fireball over Kola Peninsula on April 19, 2014 Followed by Successful Meteorite Recovery Campaign. *Meteoritics & Planetary Science* 49(1800): 5369. http://ui.adsabs.harvard.edu/abs/2014LPICo1800.5369G/abstract

Gritsevich, M., Lyytinen, E., Moilanen, J., Kohout, T., Dmitriev, V., Lupovka, V., Midtskogen, V., Kruglikov, N., et al. 2014. First Meteorite Recovery Based on Observations by the Finnish Fireball Network. In *Proceedings of the International Meteor Conference*, edited by J.-L. Rault, and P. Roggemans, 162–69. Giron, France: International Meteor Organization.

Gritsevich, M., Moilanen, J., Visuri, J., Meier, M. M. M., Maden, C., Oberst, J., Heinlein, D., et al. 2024. The Fireball of November 24, 1970, as the Most Probable Source of the Ischgl Meteorite. *Meteoritics & Planetary Science* 59: 1658–91. https://doi.org/10.1111/MAPS.14173.

Hanna, R. D., and Ketcham, R. A. 2017. X-Ray Computed Tomography of Planetary Materials: A Primer and Review of Recent Studies. *Geochemistry* 77: 547–572.

Hanna, R. D., Ketcham, R. A., Edey, D. R., and O'Connell, J. 2022. 3D Porosity Structure of the Earliest Solar System Material. *Scientific Reports* 12: 1–8.

Hanna, R. D., Ketcham, R. A., Zolensky, M., and Behr, W. M. 2015. Impact-Induced Brittle Deformation, Porosity Loss, and Aqueous Alteration in the Murchison CM Chondrite. *Geochimica et Cosmochimica Acta* 171: 256–282.

Hertz, J., Ebel, D., and Weisberg, W. 2003. Tomographic Study of Shapes and Metal Abundances of Renazzo Chondrules. *34th Lunar and Planetary Science Conference*.

Huffman, A. R., and Reimold, W. U. 1996. Experimental Constraints on Shock-Induced Microstructures in Naturally Deformed Silicates. *Tectonophysics* 256: 165–217.

Hugo, R. C., Ruzicka, A. M., and Rubin, A. E. 2020. Mesoscale and Microscale Shock Effects in the LL 6 S4 Chondrites Saint-Séverin and Elbert: A Tale of Two Breccias. *Meteoritics & Planetary Science* 55: 1418–38.

Jamsja, N., and Ruzicka, A. 2010. Shock and Thermal History of Northwest Africa 4859, an Annealed Impact-Melt Breccia of LL Chondrite Parentage Containing Unusual Igneous Features and Pentlandite. *Meteoritics & Planetary Science* 45: 828–849. https://doi.org/10.1111/j.1945-5100.2010.01056.x.

Jenniskens, P. 2018. Review of Asteroid-Family and Meteorite-Type Links. *Proceedings of the International Astronomical Union* 14(A30): 9–12.

Jung, H., Katayama, I., Jiang, Z., Hiraga, T., and Karato, S.-I. 2006. Effect of Water and Stress on the Lattice-Preferred Orientation of Olivine. *Tectonophysics* 421: 1–22. https://doi.org/10.1016/j.tecto.2006.02.011.

Kallemeyn, G. W., Rubin, A. E., Wang, D., and Wasson, J. T. 1989. Ordinary Chondrites: Bulk Compositions, Classification, Lithophile-Element Fractionations and Composition-Petrographic Type Relationships. *Geochimica et Cosmochimica Acta* 53: 2747–67.

Karato, S.-I., Jung, H., Katayama, I., and Skemer, P. 2008. Geodynamic Significance of Seismic Anisotropy of the Upper Mantle: New Insights from Laboratory Studies. *Annual Review of Earth and Planetary Sciences* 36: 59–95. https://doi.org/10.1146/annurev.earth.36.031207.124120.

Kartashova, A., Golubaev, A., Mozgova, A., Chuvashov, I., Bolgova, G., Glazachev, D., and Efremov, V. 2020. Investigation of the Ozerki Meteoroid Parameters. *Planetary and Space Science* 193: 105034.

Ketcham, R. A., and Carlson, W. D. 2001. Acquisition, Optimization and Interpretation of X-Ray Computed Tomographic Imagery: Applications to the Geosciences. *Computers and Geosciences* 27: 381–400.

King, A. J., Daly, L., Rowe, J., Joy, K. H., Greenwood, R. C., Devillepoix, H. A. R., Suttle, M. D., et al. 2022. The Winchcombe Meteorite, a Unique and Pristine Witness from the Outer Solar System. *Science Advances* 8: 3925. https://doi.org/10.1126/sciadv.abq3925.

Kohout, T., Gritsevich, M., Grokhovsky, V., Yakovlev, G., Haloda, J., Halodova, P., Michallik, R., Penttilä, A., and Muinonen, K. 2014. Mineralogy, Reflectance Spectra, and Physical Properties of the Chelyabinsk LL5 Chondrite—Insight into Shock-Induced Changes in Asteroid Regoliths. *Icarus* 228: 78–85. https://doi.org/10.1016/j.icarus.2013.09.027.

Kohout, T., Haloda, J., Halodová, P., Meier, M. M. M., Maden, C., Busemann, H., Laubenstein, M., et al. 2017. Annama H Chondrite—Mineralogy, Physical Properties, Cosmic Ray Exposure, and Parent Body History. *Meteoritics & Planetary Science* 52: 1525–41. https://doi.org/10.1111/maps.12871.

Korochantseva, E., Verchovsky, A., Buikin, A., Lorents, K., and Korochantsev, A. 2020. Isotopic Composition of Noble Gases, Nitrogen, and Carbon in the Ozerki New L Chondrite. *Geochemistry International* 58: 1239–56. https://doi.org/10.1134/s0016702920110075.

Krzesińska, A. 2011. High Resolution X-Ray Tomography as a Tool for Analysis of Internal Textures in Meteorites. *Meteorites* 1: 3–12.

Kyrylenko, I., Golubov, O., Slyusarev, I., Visuri, J., Gritsevich, M., Krugly, Y. N., Belskaya, I., and Shevchenko, V. G. 2023. The First Instrumentally Documented Fall of an Iron Meteorite: Orbit and Possible Origin. *The Astrophysical Journal* 953: 20. https://doi.org/10.3847/1538-4357/acdc21.

Lindgren, P., Hanna, R. D., Dobson, K. J., Tomkinson, T., and Lee, M. R. 2015. The Paradox between Low Shock-Stage and Evidence for Compaction in CM Carbonaceous Chondrites Explained by Multiple Low-Intensity Impacts. *Geochimica et Cosmochimica Acta* 148: 159–178.

Luo, Y., Chen, H., Beard, S., Zeng, X., Hu, S., Du, Z., et al. 2024. EBSD Analysis of Iron-Nickel Metal in L Type Ordinary Chondrites: 1. The Microstructural Shock Signatures. *Journal of Geophysical Research: Planets* 129: e2023JE007938. https://doi.org/10.1029/2023JE007938.

Lyytinen, E., and Gritsevich, M. 2013. A Flexible Fireball Entry Track Calculation Program. In *Proceedings of the International Meteor Conference 2012*, edited by M.

Gyssens, and P. Roggemans, 155–167. Hove: International Meteor Organization.

Lyytinen, E., and Gritsevich, M. 2016a. Calibration of Occasionally Taken Images Using Principles of Perspective. In *Proceedings of the International Meteor Conference 2016*, edited by A. Roggemans, and P. Roggemans, 159–163. Hove: International Meteor Organization.

Lyytinen, E., and Gritsevich, M. 2016b. Implications of the Atmospheric Density Profile in the Processing of Fireball Observations. *Planetary and Space Science* 120: 35–42. https://doi.org/10.1016/j.pss.2015.10.012.

Maksimova, A., Petrova, E., Chukin, A., Karabanalov, M., Felner, I., Gritsevich, M., and Oshtrakh, M. 2020. Characterization of the Matrix and Fusion Crust of the Recent Meteorite Fall Ozerki L6. *Meteoritics & Planetary Science* 55: 231–244. https://doi.org/10.1111/maps.13423.

Martell, J., Alwmark, C., Daly, L., Hall, S., Alwmark, S., Woracek, R., Hektor, J., Helfen, L., Tengattini, A., and Lee, M. 2022. The Scale of a Martian Hydrothermal System Explored Using Combined Neutron and x-Ray Tomography. *Science Advances* 8: eabn3044.

McCarroll, I. E., Daly, L., White, L. F., et al. 2022. Atom Probe Tomography and Correlative Microscopy: Key Techniques for Future Planetary Science Studies. *MRS Bulletin* 47: 696–705. https://doi.org/10.1557/s43577-022-00375-6.

Meier, M. M. M., Welten, K. C., Riebe, M. E. I., Caffee, M. W., Gritsevich, M., Maden, C., and Busemann, H. 2017. Park Forest (L5) and the Asteroidal Source of Shocked L Chondrites. *Meteoritics & Planetary Science* 52: 1561–76. https://doi.org/10.1111/maps.12874.

Miyahara, M., Tomioka, N., and Bindi, L. 2021. Natural and Experimental High-Pressure, Shock-Produced Terrestrial and Extraterrestrial Materials. *Progress in Earth and Planetary Science* 8: 1–26. https://doi.org/10.1186/s40645-021-00451-6.

Moilanen, J., Gritsevich, M., and Lyytinen, E. 2021. Determination of Strewn Fields for Meteorite Falls. *Monthly Notices of the Royal Astronomical Society* 503: 3337–50. https://doi.org/10.1093/mnras/stab586.

Pastukhovich, A. Y., Yakovlev, G. A., Petrova, E. V., Gritsevich, M. I., Lyytinen, E., Sharygin, V. V., Zamyatin, D. A., Larionov, M. Y., Kruglikov, N. A., and Grokhovsky, V. I. 2019. Meteorite Ozerki: From Fall to Registration. Minerals: Structure, Properties. *Methods of Investigations* 10: 185–87 (In Russian).

Paterson, S. R., Fowler Jr, T. K., Schmidt, K. L., Yoshinobu, A. S., Yuan, E. S., and Miller, R. B. 1998. Interpreting Magmatic Fabric Patterns in Plutons. *Lithos* 44: 53–82.

Peña-Asensio, E., Trigo-Rodríguez, J. M., Gritsevich, M., and Rimola, A. 2021. Accurate 3D Fireball Trajectory and Orbit Calculation using the 3D-Firetoc Automatic Python Code. *Monthly Notices of the Royal Astronomical Society* 504: 4829–40. https://doi.org/10.1093/mnras/stab999.

Perona, P., and Malik, J. 1990. Scale-Space and Edge Detection Using Anisotropic Diffusion. *IEEE Transactions on Pattern Analysis and Machine Intelligence* 12: 629–639. https://doi.org/10.1109/34.56205.

Rubin, A. E. 2002. Post-Shock Annealing of Miller Range 99301 (LL6): Implications for Impact Heating of Ordinary Chondrites. *Geochimica et Cosmochimica Acta* 66: 3327–37.

Russell, S. S., King, A. J., Bates, H. C., Almeida, N. V., Greenwood, R. C., Daly, L., Joy, K. H., et al. 2023.

Recovery and Curation of the Winchcombe (CM2) Meteorite. *Meteoritics & Planetary Science* 59: 973–987. https://doi.org/10.1111/maps.13956.

Ruzicka, A. M., Friedrich, J. M., Hutson, M. L., Strasser, J. W., Macke, R. J., Rivers, M. L., Greenwood, R. C., Ziegler, K., and Pugh, R. N. 2020. Shock Compaction Heating and Collisional Processes in the Production of Type 3 Ordinary Chondrites: Lessons from the (Nearly) Unique L3 Chondrite Melt Breccia Northwest Africa 8709*. *Meteoritics & Planetary Science* 55: 2117–40. https://doi.org/10.1111/maps.13567.

Ruzicka, A. M., Hugo, R. C., Friedrich, J. M., and Ream, M. T. 2024. Accretion of Warm Chondrules in Weakly Metamorphosed Ordinary Chondrites and their Subsequent Reprocessing. *Geochimica et Cosmochimica Acta* 378: 1–35.

Ruzicka, A., and Hugo, R. C. 2018. Electron Backscatter Diffraction (EBSD) Study of Seven Heavily Metamorphosed Chondrites: Deformation Systematics and Variations in Pre-Shock Temperature and Post-Shock Annealing. *Geochimica et Cosmochimica Acta* 234: 115–147. https://doi.org/10.1016/j.gca.2018.05.014.

Ruzicka, A., Brown, R., Friedrich, J., Hutson, M., Hugo, R., and Rivers, M. 2015. Shock-Induced Mobilization of Metal and Sulfide in Planetesimals: Evidence from the Buck Mountains 005 (L6 S4) Dike-Bearing Chondrite. *American Mineralogist* 100: 2725–38.

Ruzicka, A., Hugo, R., and Hutson, M. 2015. Deformation and Thermal Histories of Ordinary Chondrites: Evidence for Post-Deformation Annealing and Syn-Metamorphic Shock. *Geochimica et Cosmochimica Acta* 163: 219–233.

Sansom, E. K., Gritsevich, M., Devillepoix, H. A. R., Jansen-Sturgeon, T., Shober, P., Bland, P. A., Towner, M. C., Cupák, M., Howie, R. M., and Hartig, B. A. D. 2019. Determining Fireball Fates Using the α-β Criterion. *The Astrophysical Journal* 885: 115. https://doi.org/10.3847/1538-4357/ab4516.

Schmitt, R. 2000. Shock Experiments with the H6 Chondrite Kernouvé: Pressure Calibration of Microscopic Shock Effects. *Meteoritics & Planetary Science* 35: 545–560.

Skemer, P., Katayama, I., Jiang, Z., and Karato, S.-i. 2005. The Misorientation Index: Development of a New Method for Calculating the Strength of Lattice-Preferred Orientation. *Tectonophysics* 411: 157–167. https://doi.org/10.1016/j.tecto.2005.08.023.

Sneddon, G. C., Trimby, P. W., and Cairney, J. M. 2016. Transmission Kikuchi Diffraction in a Scanning Electron Microscope: A Review. *Materials Science and Engineering: R: Reports* 110: 1–12.

Stöffler, D., Hamann, C., and Metzler, K. 2018. Shock Metamorphism of Planetary Silicate Rocks and Sediments: Proposal for an Updated Classification System. *Meteoritics & Planetary Science* 53: 5–49.

Stöffler, D., Keil, K., and Scott, E. R. D. 1991. Shock Metamorphism of Ordinary Chondrites. *Geochimica et Cosmochimica Acta* 55: 3845–67. https://doi.org/10.1016/0016-7037(91)90078-J.

Tait, A. W., Tomkins, A. G., Godel, B. M., Wilson, S., and Hasalova, P. 2014. Investigation of the H7 Ordinary Chondrite, Watson 012: Implications for Recognition and Classification of Type 7 Meteorites. *Geochimica et Cosmochimica Acta* 134: 175–196.

Tomeoka, K., Yamahana, Y., and Sekine, T. 1999. Experimental Shock Metamorphism of the Murchison CM Carbonaceous

Chondrite. *Geochimica et Cosmochimica Acta* 63: 3683–3703. https://doi.org/10.1016/s0016-7037(99)00149-0.

Trigo-Rodríguez, J. M., Lyytinen, E., Gritsevich, M., Moreno-Ibáñez, M., Bottke, W. F., Williams, I., Lupovka, V., Dmitriev, V., Kohout, T., and Grokhovsky, V. 2015. Orbit and Dynamic Origin of the Recently Recovered Annama's H5 Chondrite. *Monthly Notices of the Royal Astronomical Society* 449: 2119–27. https://doi.org/10.1093/mnras/stv378.

Vollmer, F. W. 1990. An Application of Eigenvalue Methods to Structural Domain Analysis. *Geological Society of America Bulletin* 102(6): 786–791. https://doi.org/10.1130/0016-7606(1990)102⟨0786:AAOEMT⟩2.3.CO;2.

Wasson, J. T. 1972. Formation of Ordinary Chondrites. *Reviews of Geophysics* 10: 711–759.

Weisberg, M. K., McCoy, T. J., and Krot, A. N. 2006. Systematics and Evaluation of Meteorite Classification. In *Meteorites and the Early Solar System II*, edited by D. S. Lauretta, and H. Y. Sween, Jr., 19–52. Univ. of Arizona Press.

Wheeler, J., Mariani, E., Piazolo, S., Prior, D. J., Trimby, P., and Drury, M. R. 2009. The Weighted Burgers Vector: A New Quantity for Constraining Dislocation Densities and Types Using Electron Backscatter Diffraction on 2D Sections through Crystalline Materials. *Journal of Microscopy* 233: 482–494. https://doi.org/10.1111/j.1365-2818.2009.03136.x.

Wheeler, J., Piazolo, S., Prior, D. J., Trimby, P. W., and Tielke, J. A. 2024. Using Crystal-Lattice Distortion Data for Geological Investigations: The Weighted Burgers Vector Method. *Journal of Structural Geology* 179: 105040. https://doi.org/10.1016/j.jsg.2023.105040.

Woodcock, N., and Naylor, M. 1983. Randomness Testing in Three-Dimensional Orientation Data. *Journal of Structural Geology* 5: 539–548. https://doi.org/10.1016/0191-8141(83)90058-5.

Zhang, A. C., Wang, R. C., Hsu, W. B., and Bartoschewitz, R. 2013. Record of S-Rich Vapors on Asteroid 4 Vesta: Sulfurization in the Northwest Africa 2339 Eucrite. *Geochimica et Cosmochimica Acta* 109: 1–13.

Zolensky, M., and Mikouchi, T. 2010. Structures of Extraterrestrial Minerals Revealed by EBSD. *Microscopy and Microanalysis* 16(S2): 676–77.

SUPPORTING INFORMATION

Additional supporting information may be found in the online version of this article.

Table S1. EBSD parameters for metal grains (diameter > 50px).

Table S2. EBSD quantitative texture metrics, including m-index, j-index, and PGR eigenvalue analysis, for olivine grains (diameter > 50px) and metal grains (diameter > 50px).

Table S3. EBSD parameters for olivine grains (diameter > 50px).

Table S4. Olivine multiples of uniform density (MUD) for each crystal rotation axis used to calculate the skewness ratio (*Sk*; previously known as, inferred annealing parameter) and the misorientation rotation parameter $R_{2\text{-}10}$ ratio (previously known as the inferred temperature parameter).